Supporting Information for "Impact of the Juan Fernandez ridge on the Pampean flat subduction inferred from full waveform inversion"

Yajian Gao[1,2], Xiaohui Yuan[1], Benjamin Heit[1], Frederik Tilmann[1,2], Dirk-Philip van Herwaarden[3], Solvi Thrastarson[3], Andreas Fichtner[3], Bernd Schurr[1]

[1]GFZ German Research Centre for Geosciences, Potsdam, Germany

[2]Freie Universität Berlin, Berlin, Germany

[3]ETH, Zürich, Switzerland

Contents of this file

Texts S1, S2 and S3, Tables S1 and S2, Figures S1 to S26

S1: Model construction and inversion working flow

Long-wavelength surface topography from the EGM2008 Geoid (Pavlis et al., 2012) and Earth2014 global topography model (Hirt & Rexer, 2015) with Earth ellipticity according to WGS84 and Moho topography from Crust1.0 (Laske et al., 2013) are implemented by deforming the mesh grid vertically. The surface and Moho topography have been filtered with maximum angular order $lmax = 128$, equivalent to a spatial resolution of 155 km. In order to constrain the deep structure of the upper mantle, we initiate our inversion from

long-period surface wave data at 60–120 s and progress in seven stages to a final period range of 12–120 s (see Table S2); the progressive extension to shorter periods mitigates the risk of falling into local minima. The model updates are driven by the Limited-Memory Broyden–Fletcher–Goldfarb–Shanno algorithm (L-BFGS Liu & Nocedal, 1989). We employ the Time-Frequency Phase Shift and Cross-Correlation-Coefficient misfits as misfit functions during stage I-V and VI-VII, respectively, following Gao et al. (2021) with the assistance of the *Large-scale Seismic Inversion Framework 2.0* (Krischer et al., 2015; Thrastarson et al., 2021). The detailed misfit evolution chart and histograms based on events and seismic traces are shown in Figure S4. Exemplary waveform fits from four events are illustrated in Figures S25-S28. More technical details about the inversion workflow can be found in Gao et al. (2021).

S2: Point-spreading tests

We analyse the resolution for the inversion and the trade-offs among the parameter types. In traditional ray theory tomography, the checkerboard test is popular and relatively robust with low computational costs, but it is computationally prohibitive for FWIs. In this study, we therefore approximate the Hessian-vector product $\mathbf{H}\delta\mathbf{m}$ for a test function $\delta\mathbf{m}$ (Fichtner & Trampert, 2011; Fichtner & Leeuwen, 2015; Zhu et al., 2015, 2017; Tao et al., 2018)

$$\mathbf{H}\delta\mathbf{m} = \mathbf{g}(\mathbf{m} + \delta\mathbf{m}) - \mathbf{g}(\mathbf{m}) \tag{1}$$

where $\mathbf{g}(\mathbf{m})$ denotes the summed gradient from the adjoint simulations for model $\mathbf{m}$, and $\mathbf{g}(\mathbf{m}+\delta\mathbf{m})$ indicates the gradient from the perturbed model $\mathbf{m}+\delta\mathbf{m}$.

If the synthetics from the final model provide a good fit of the observed data and the inversion thus has reached convergence, $\mathbf{H}\delta\mathbf{m}$ can be used to estimate the model resolution. Specifically, when the $\delta\mathbf{m}$ is nearly point-localised, the $\mathbf{H}\delta\mathbf{m}$ will be a linearised point-spread function.

In order to provide a visual representation of resolution throughout the model rather than just for a single model node, we perturbed our model by adding velocity perturbations $\delta\mathbf{m}$ in a three dimensional checkerboard pattern in the upper mantle made up of Gaussian spheres with $\pm 1\%$ maximum amplitude of the velocity for a specific depth and a Gaussian radius σ of 40 km. The horizontal and depth grid spacing of the Gaussian spheres are 2° and 100 km (Figure S17). We calculate $\mathbf{H}\delta\mathbf{m}$ for this anomaly pattern for V_{SV}, V_{SH} and isotropic V_P separately (Figure S17-S19).

Through the multi-parameter point-spread tests, we could confirm that the resolution for the inversion parameters is mostly confined to the top 400 km, although V_{SV} and isotropic V_P even show some ability to resolve the structure down to 460 km. The resolution of V_{SH} is confined to 360 km depth. Therefore, we could extend our interpretation on both of the isotropic V_S and V_P down to about 400 km.

To further quantitatively assess the resolution, we also present the normalised product of the perturbations $\delta\mathbf{m}$ and the resultant Hessian product $\mathbf{H}\delta\mathbf{m}$ within and between parameter classes (Figure S12-S14).

S3: Model comparison

In this section, we provide a simple comparison (Figure S17) between our model with (Ward et al., 2013). Although the shape of the recovered anomalies is sometimes quite

different, the basic features can generally be found in both models. For example, the forearc has higher velocities than the main volcanic arc, indicating colder temperatures. Importantly, in the middle crust (20 km) only moderately low velocities are found from 29°S to 32°S and spread over a wider distance in EW-direction, compared to the segments north and south with stronger anomalies confined to the active volcanic arc. In general, the anomalies imaged by us tend to be more focused and with larger amplitudes, compared to Ward et al. (2013).

References

Albuquerque Seismological Laboratory (ASL)/USGS. (1988). *Global Seismograph Network (GSN - IRIS/USGS).* International Federation of Digital Seismograph Networks. doi: https://doi.org/10.7914/SN/IU

Albuquerque Seismological Laboratory (ASL)/USGS. (1993). *Global Telemetered Seismograph Network (USAF/USGS).* International Federation of Digital Seismograph Networks. doi: https://doi.org/10.7914/SN/GT

Asch, G., Heit, B., & Yuan, X. (2002). *The ReFuCA project: Receiver Functions Central Andes.* GFZ Data Services.

Beck, L., Susan, & Terry, W. (2000). *Slab Geometry in the Southern Andes.* International Federation of Digital Seismograph Networks. Retrieved from `http://www.fdsn.org/doi/10.7914/SN/YC_2000` doi: https://doi.org/10.7914/SN/YC_2000

Beck, L., Susan, & Zandt, G. (2007). *Lithospheric Structure and Deformation of the Flat Slab Region of Argentina.* International Federation of Digital Seismograph Networks. doi: https://doi.org/10.7914/SN/ZL_2007

Dziewonski, A. M., & Anderson, D. L. (1981). Preliminary reference Earth model. *Physics of the Earth and Planetary Interiors*, *25*(4), 297 - 356. doi: https://doi.org/10.1016/0031-9201(81)90046-7

Fichtner, A., & Leeuwen, T. v. (2015). Resolution analysis by random probing. *Journal of Geophysical Research: Solid Earth*, *120*(8), 5549-5573. doi: https://doi.org/10.1002/2015JB012106

Fichtner, A., & Trampert, J. (2011). Resolution analysis in full waveform inversion. *Geophysical Journal International*, *187*(3), 1604–1624. doi: https://doi.org/10.1111/j.1365-246X.2011.05218.x

Gao, Y., Tilmann, F., van Herwaarden, D.-P., Thrastarson, S., Fichtner, A., Heit, B., ... Schurr, B. (2021). Full Waveform Inversion beneath the Central Andes: Insight into the dehydration of the Nazca slab and delamination of the back-arc lithosphere. *Journal of Geophysical Research: Solid Earth*, *126*(7), e2021JB021984. doi: https://doi.org/10.1029/2021JB021984

GFZ, & CNRS-INSU. (2006). *IPOC Seismic Network.* Integrated Plate boundary Observatory Chile - IPOC. doi: https://doi.org/10.14470/PK615318

Hayes, G. P., Moore, G. L., Portner, D. E., Hearne, M., Flamme, H., Furtney, M., & Smoczyk, G. M. (2018). Slab2, a comprehensive subduction zone geometry model. *Science*, *362*(6410), 58–61. doi: https://doi.org/10.1126/science.aat4723

Heit, B., Yuan, X., Kind, R., & Asch, G. (2007). *Lithospheric dynamics in the southernmost Andean Plateau (PUDEL).* GFZ Data Services. doi: https://doi.org/10.14470/7O092361

Hersh, Gilbert. (2008). *Eastern Sierras Pampeanas, Lithospheric Structure above the variably dipping Nazca Slab.* International Federation of Digital Seismograph Networks. doi: https://doi.org/10.7914/SN/XH_2008

Hirt, C., & Rexer, M. (2015). Earth2014: 1 arc-min shape, topography, bedrock and ice-sheet models – Available as gridded data and degree-10,800 spherical harmonics. *International Journal of Applied Earth Observation and Geoinformation*, *39*, 103 - 112. doi: https://doi.org/10.1016/j.jag.2015.03.001

IPGP, & EOST. (1982). *GEOSCOPE, French Global Network of broad band seismic stations.* Institut de physique du globe de Paris (IPGP), Université de Paris. Retrieved from `http://geoscope.ipgp.fr/networks/detail/G/` doi: https://doi.org/10.18715/GEOSCOPE.G

Krischer, L., Fichtner, A., Zukauskaite, S., & Igel, H. (2015). Large?scale seismic inversion framework. *Seismological Research Letters*, *86*(4), 1198. Retrieved from `http://dx.doi.org/10.1785/0220140248` doi: https://doi.org/10.1785/0220140248

Lange, D., Cembrano, J., & Sielfeld, G. (2019). *Crustal Seismicity along for the Southern Andes Volcanic Zone (LOFS).* GFZ Data Services. doi: https://doi.org/10.14470/8U7569253520

Laske, G., Masters, G., Ma, Z., & Pasyanos, M. (2013). Update on CRUST1. 0—A 1-degree global model of Earth's crust. In *Geophys. Res. Abstracts, 15, Abstract EGU2013-2658.*

Liu, D. C., & Nocedal, J. (1989, Aug 01). On the limited memory bfgs method for large scale optimization. *Mathematical Programming*, *45*(1), 503–528. Retrieved from

https://doi.org/10.1007/BF01589116 doi: 10.1007/BF01589116

Pavlis, N. K., Holmes, S. A., Kenyon, S. C., & Factor, J. K. (2012). The development and evaluation of the Earth Gravitational Model 2008 (EGM2008). *Journal of Geophysical Research: Solid Earth*, *117*(B4). doi: https://doi.org/10.1029/2011JB008916

Rietbrock, A., Haberland, C., Bataille, K., Lange, D., & Dahm, T. (2004). *TIPTEQ-Temporary seismological network (North) (2004/2005).* GFZ Data Services. doi: https://doi.org/10.14470/MJ7559637482

Ritsema, J., van Heijst, H. J., & Woodhouse, J. H. (1999). Complex shear wave velocity structure imaged beneath Africa and Iceland. *Science*, *286*(5446), 1925–1928. doi: https://doi.org/10.1126/science.286.5446.1925

Rivadeneyra-Vera, C., Bianchi, M., Assumpção, M., Cedraz, V., Julià, J., Rodríguez, M., ... others (2019). An updated crustal thickness map of central South America based on receiver function measurements in the region of the Chaco, Pantanal, and Paraná Basins, southwestern Brazil. *Journal of Geophysical Research: Solid Earth*, *124*(8), 8491–8505. doi: https://doi.org/10.1029/2018JB016811

Sandvol, E., & Brown, L. (2007). *SLIP—Seismic Lithospheric Imaging of the Puna Plateau.* International Federation of Digital Seismograph Networks. doi: https://doi.org/10.7914/SN/X6_2007

Schurr, B., Asch, G., & Wigger, P. (1997). *PUNA Project.* GFZ Data Services. doi: https://doi.org/10.14470/MO6442843258

Sippl, C., Moreno, M., & Benavente, R. (2020). Microseismicity appears to outline highly coupled regions on the Central Chile megathrust. *EarthArXiv*. doi: https://doi.org/

10.31223/X56S3B

Steve Roecker, R. R. (2010). *RAMP response for 2010 earthquake.* International Federation of Digital Seismograph Networks. Retrieved from `http://www.fdsn.org/doi/10.7914/SN/XY_2010` doi: https://doi.org/10.7914/SN/XY_2010

Tao, K., Grand, S. P., & Niu, F. (2018). Seismic Structure of the Upper Mantle Beneath Eastern Asia From Full Waveform Seismic Tomography. *Geochemistry, Geophysics, Geosystems*, *19*(8), 2732-2763. doi: https://doi.org/10.1029/2018GC007460

Thrastarson, S., van Herwaarden, D. P., Krischer, L., & Fichtner, A. (2021). LASIF: Large-scale Seismic Inversion Framework, an updated version.
doi: https://doi.org/10.31223/X5NC84

Thurber, C. (2015). *Laguna del Maule seismic imaging.* International Federation of Digital Seismograph Networks. doi: https://doi.org/10.7914/SN/ZR_2015

Universidad De Chile. (2013). *Red Sismologica Nacional.* International Federation of Digital Seismograph Networks. doi: https://doi.org/10.7914/SN/C1

Vilotte, J., et al. (2011). *Seismic network XS: CHILE MAULE aftershock temporary experiment (RESIF-SISMOB).* RESIF-Réseau Sismologique et géodésique Français. doi: https://doi.org/10.15778/RESIF.XS2010

Waite, G. P. (2010). *An Integrated Analysis of Low-Frequency Seismicity at Villarrica Volcano, Chile.* International Federation of Digital Seismograph Networks. doi: https://doi.org/10.7914/SN/YM_2010

Ward, K. M., Porter, R. C., Zandt, G., Beck, S. L., Wagner, L. S., Minaya, E., & Tavera, H. (2013). Ambient noise tomography across the Central Andes. *Geophysical Journal*

International, *194*(3), 1559-1573. doi: https://doi.org/10.1093/gji/ggt166

Zhu, H., Bozdağ, E., & Tromp, J. (2015). Seismic structure of the European upper mantle based on adjoint tomography. *Geophysical Journal International*, *201*(1), 18–52. doi: https://doi.org/10.1093/gji/ggu492

Zhu, H., Komatitsch, D., & Tromp, J. (2017). Radial anisotropy of the North American upper mantle based on adjoint tomography with USArray. *Geophysical Journal International*, *211*(1), 349-377. doi: https://doi.org/10.1093/gji/ggx305

Table S1. Seismic Network information

Code	Data Center	start	end	reference
C	IRISDMC	2007	2009	Chilean National Seismic Network
*C*1	IRISDMC	2012	-	Universidad De Chile (2013)
CX	GEOFON	2006	-	GFZ and CNRS-INSU (2006)
GT	IRISDMC	1993	-	Albuquerque Seismological Laboratory (ASL)/USGS (1993)
IU	IRISDMC	1988	-	Albuquerque Seismological Laboratory (ASL)/USGS (1988)
WA	IRISDMC	2011	-	West Central Argentina Network
2*B*	GEOFON	2007	2009	Heit et al. (2007)
3*A*	IRISDMC	2010	2012	Maule Aftershock Deployment (UK)
3*H*	GEOFON	2014	2015	Lange et al. (2019)
G	IPGP	1982	-	IPGP and EOST (1982)
*X*6	IRISDMC	2007	2009	Sandvol and Brown (2007)
XH	IRISDMC	2008	2010	Hersh, Gilbert (2008)
XS	RESIF	2010	2011	Vilotte et al. (2011)
XY	IRISDMC	2010	2010	Steve Roecker (2010)
YC	IRISDMC	2002	2002	Beck and Terry (2000)
YM	IRISDMC	2010	2012	Waite (2010)
ZA	GEOFON	2002	2004	Asch et al. (2002)
ZB	GEOFON	1997	1997	Schurr et al. (1997)
ZE	GEOFON	2010	2011	Maule Aftershock Survey-GFZ
ZL	IRISDMC	2007	2009	Beck and Zandt (2007)
ZP	GEOFON	1999	2001	ISSA Southern Andes
ZQ	GEOFON	2004	2005	Cerro Blanco Project Central Andes
ZR	IRISDMC	2015	2018	Thurber (2015)
ZW	GEOFON	2005	2005	Rietbrock et al. (2004)

Table S2. Overview of inversion stages. TF: Time Frequency, CCC: Cross Correlation Coefficient

No.	Periods	It.	Simulation time	Events	Windows	Misfit
I	60–120 s	5	450 s	71	7785	TF
II	40–120 s	7	450 s	93	10211	TF
III	30–100 s	7	450 s	93	12497	TF
IV	20–100 s	11	450 s	93	12497	TF
V	20–100 s	7	450 s	110	28399	TF
VI	15–100 s	9	450 s	120	61516	CCC
VII	12–100 s	8	450 s	139	74751	CCC

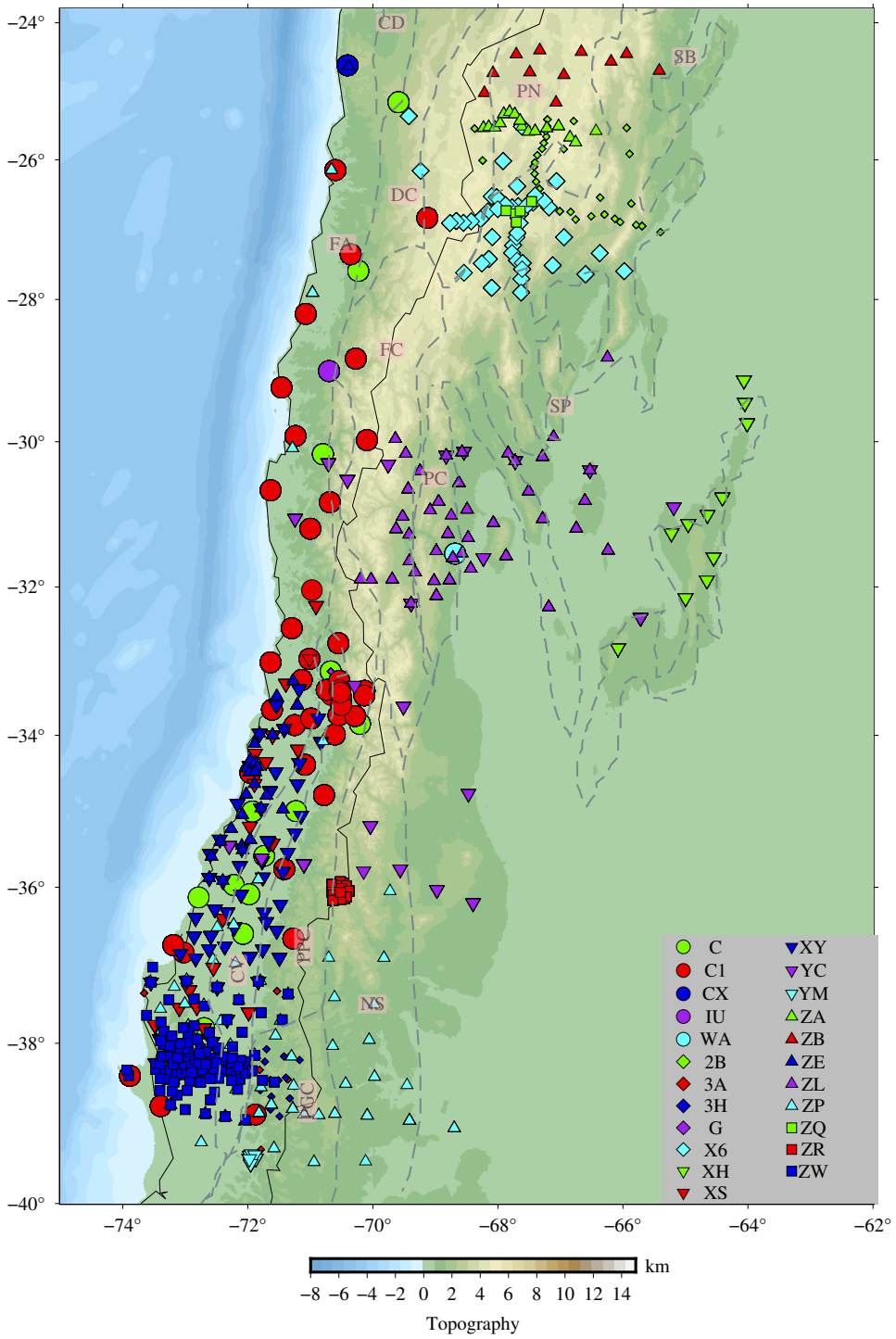

Figure S1. Map showing seismic stations of individual networks used in the study with circles marking the permanent stations. Detailed information about the networks is given in Table S1

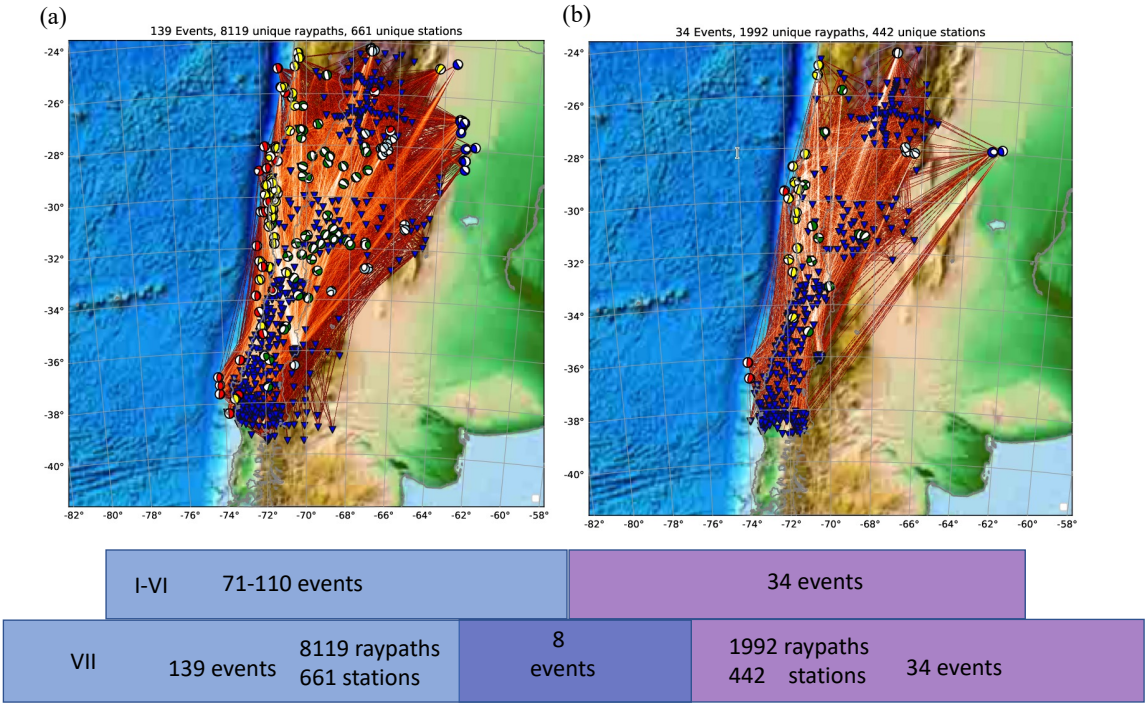

Figure S2. (a) Earthquakes, stations and ray-paths used for the inversion. (b) Earthquakes, stations and ray-paths for the validation dataset. 8 earthquakes are overlapped between the inversion data set and validation data set in the final inversion stage (VII). The waveforms in the validation dataset were not used in the inversion, but instead used to evaluate improvement of the model and avoid overfitting. See Fig. S4 for a comparison of fit improvements in inversion and validation dataset.

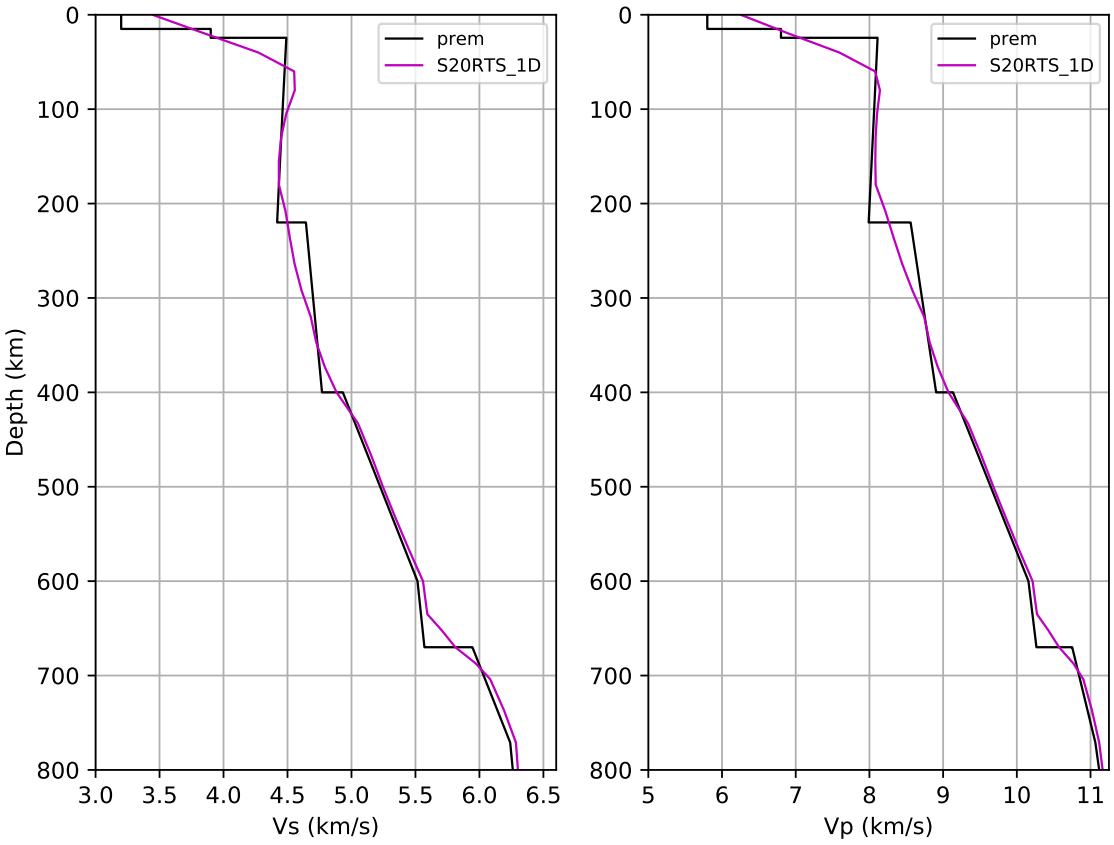

Figure S3. The reference 1D model derived from the depth-averaged initial S20RTS (Ritsema et al., 1999) model, compared with isotropic PREM (Dziewonski & Anderson, 1981).

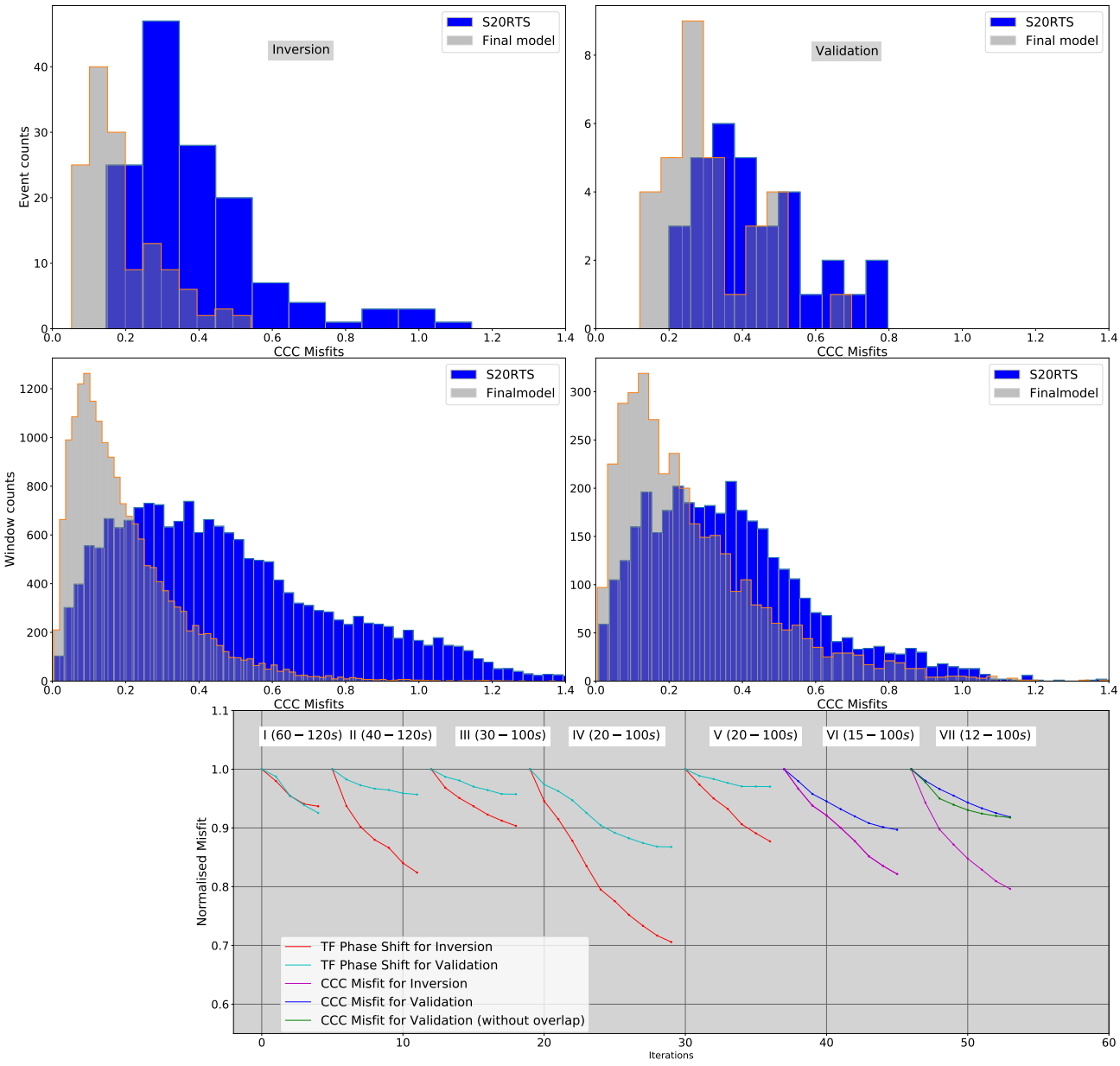

Figure S4. Top: Histogram of average cross corrrelation coefficient (CCC) misfits for each event for the starting model and after the final iteration; the left column shows the inversion, the right column the validation data set. Middle: Histogram of CCC misfits for each trace; Lower: Misfit evolution with iterations. See Fig. S2 for more details on inversion and validation dataset.

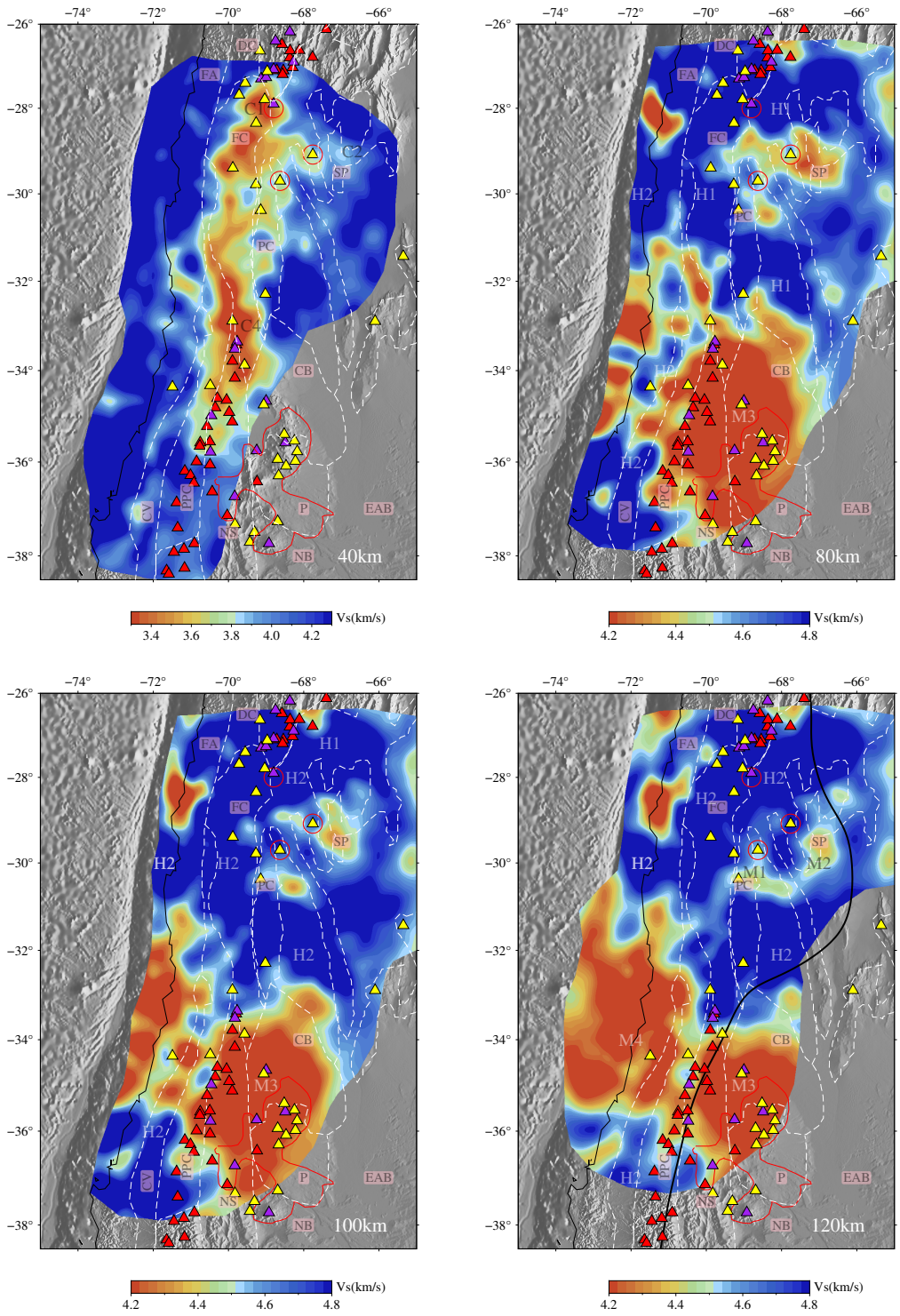

Figure S5. Horizontal slices for isotropic V_S model at 40 km, 80 km, 100 km and 120 km depth.

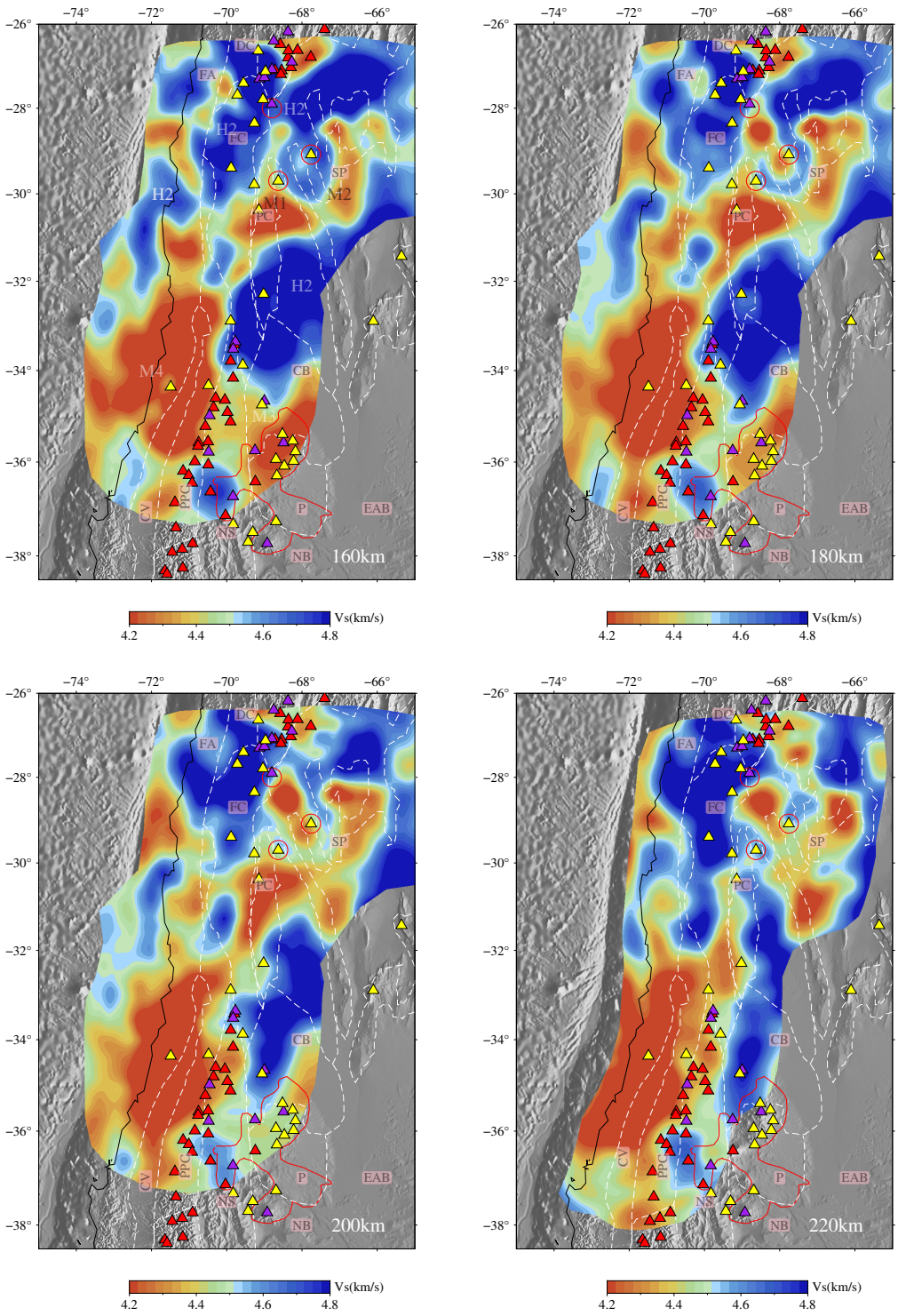

Figure S6. Horizontal slices for isotropic V_S model at 160 km, 180 km, 200 km and 220 km depth.

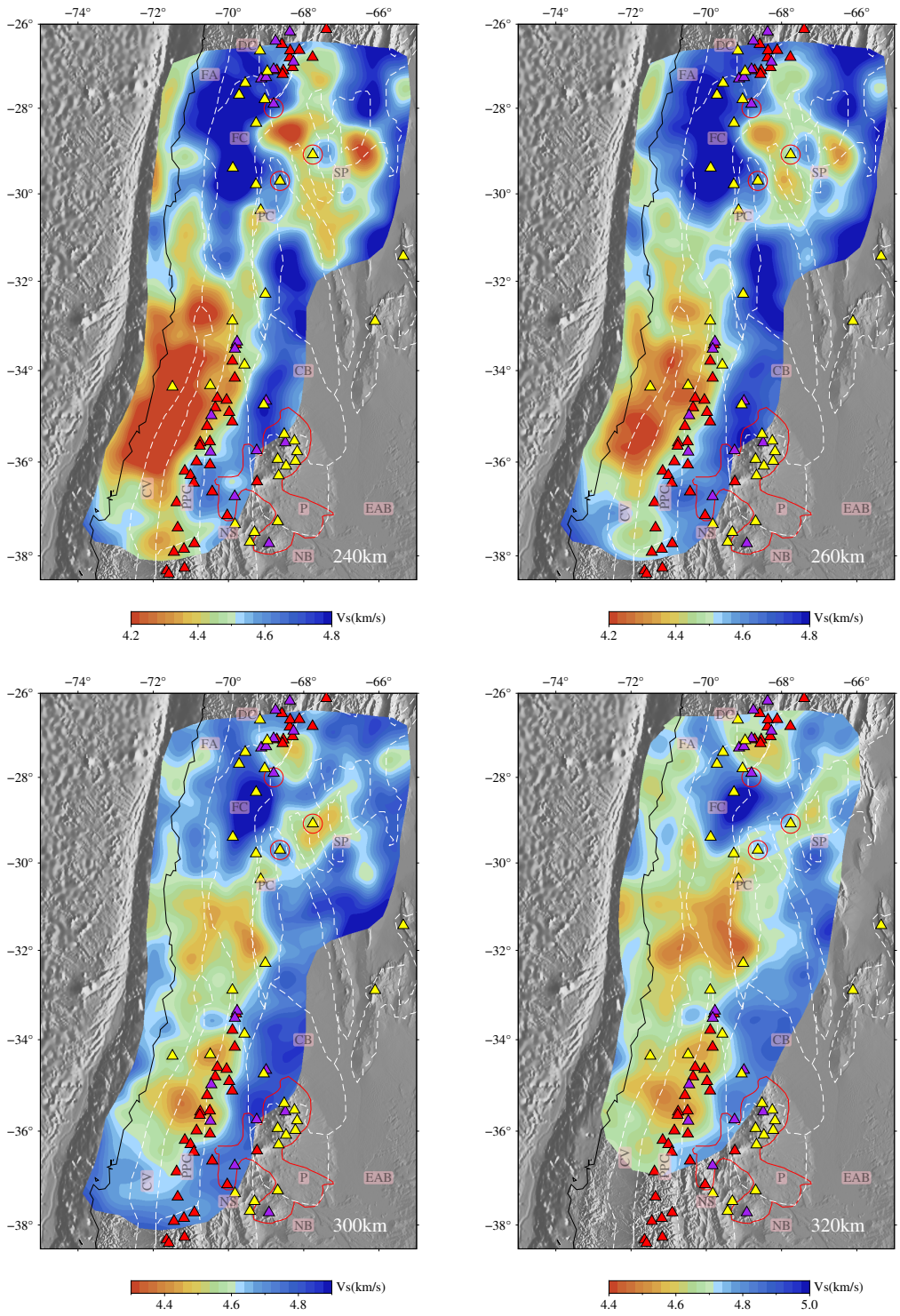

Figure S7. Horizontal slices for isotropic V_S model at 240 km, 260 km, 300km and 320 km depth.

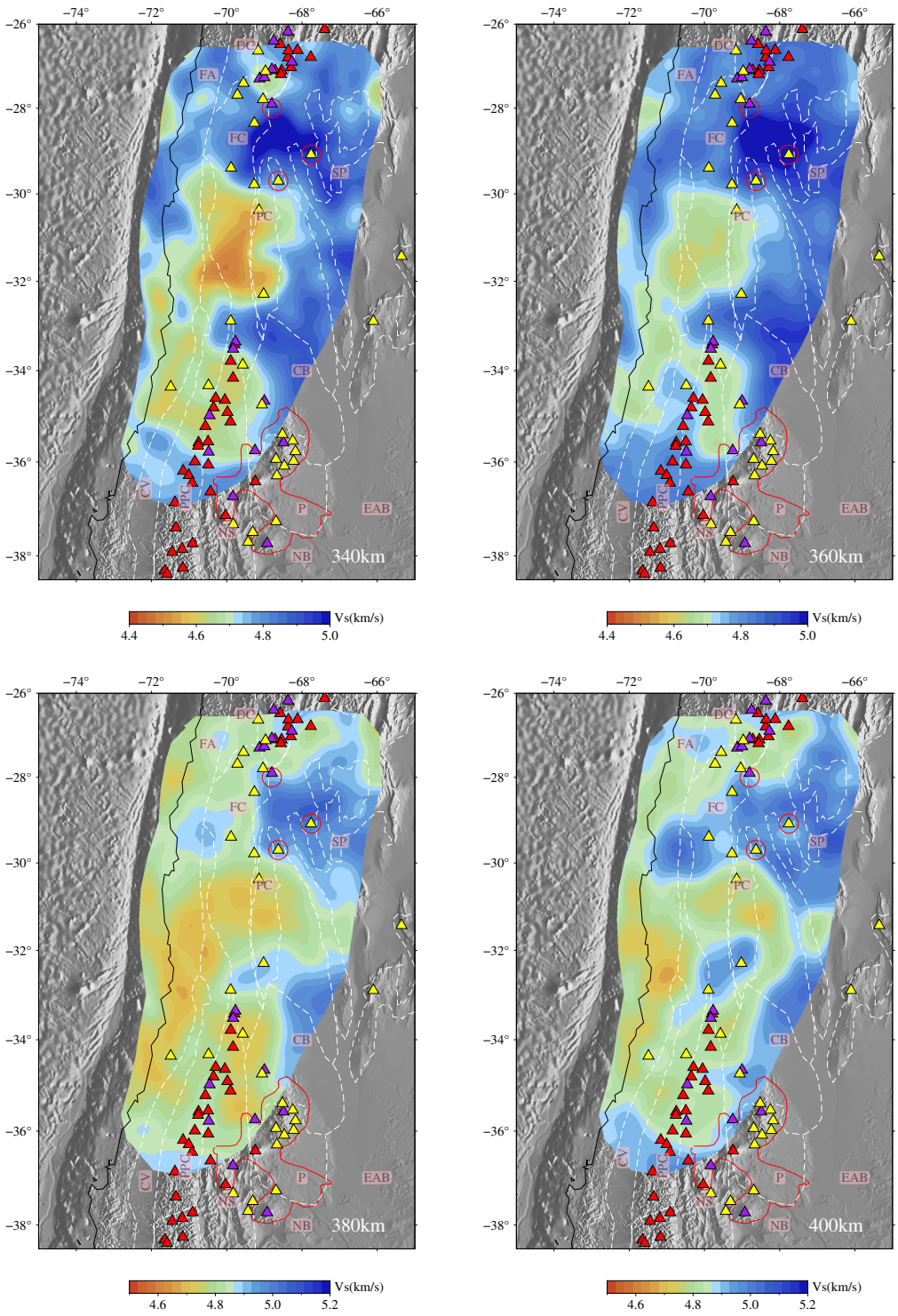

Figure S8. Horizontal slices for isotropic V_S model at 340 km, 360 km, 380 km and 400 km depth.

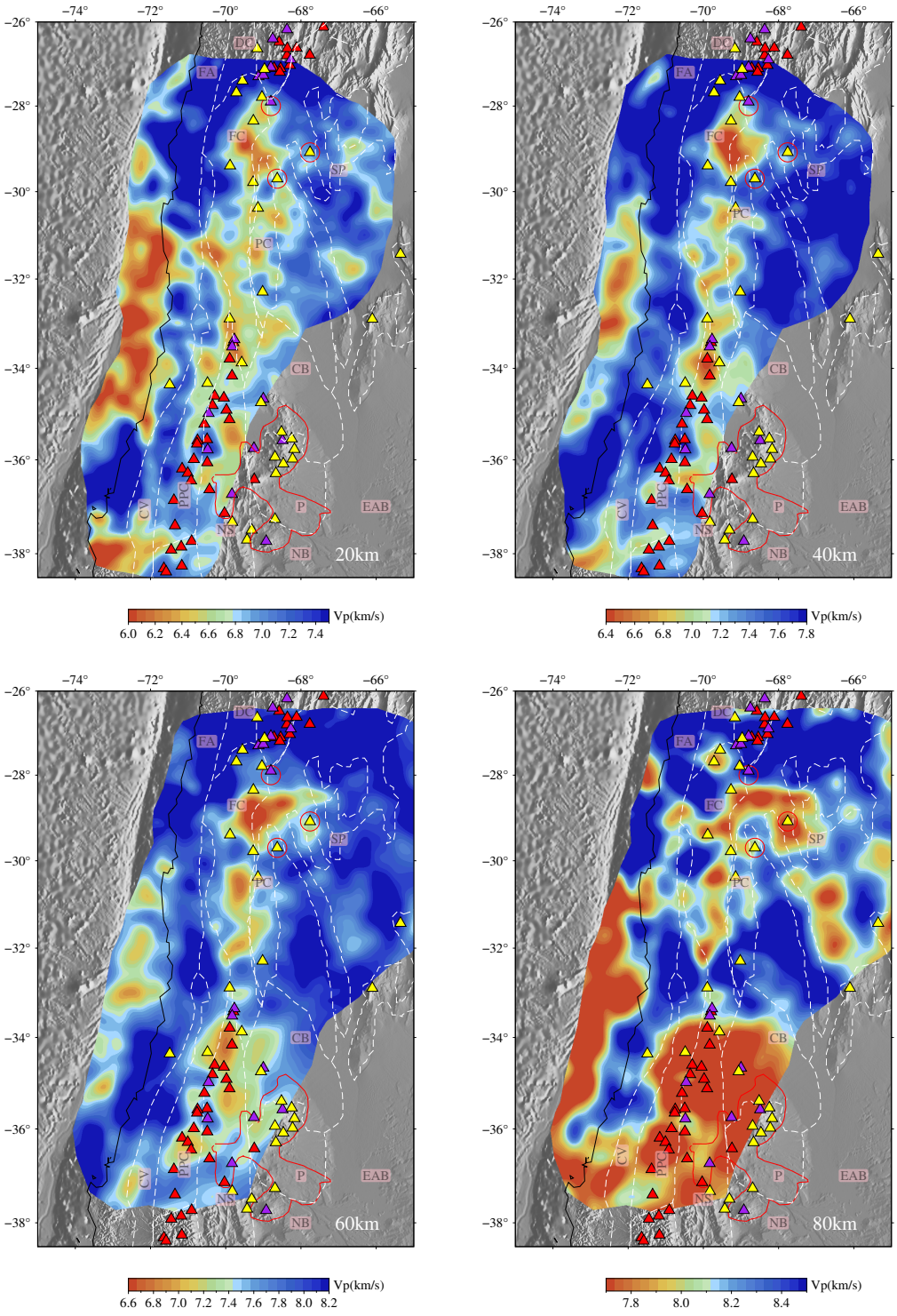

Figure S9. Horizontal slices for isotropic V_P model at 20 km, 40 km, 60 km and 80 km depth.

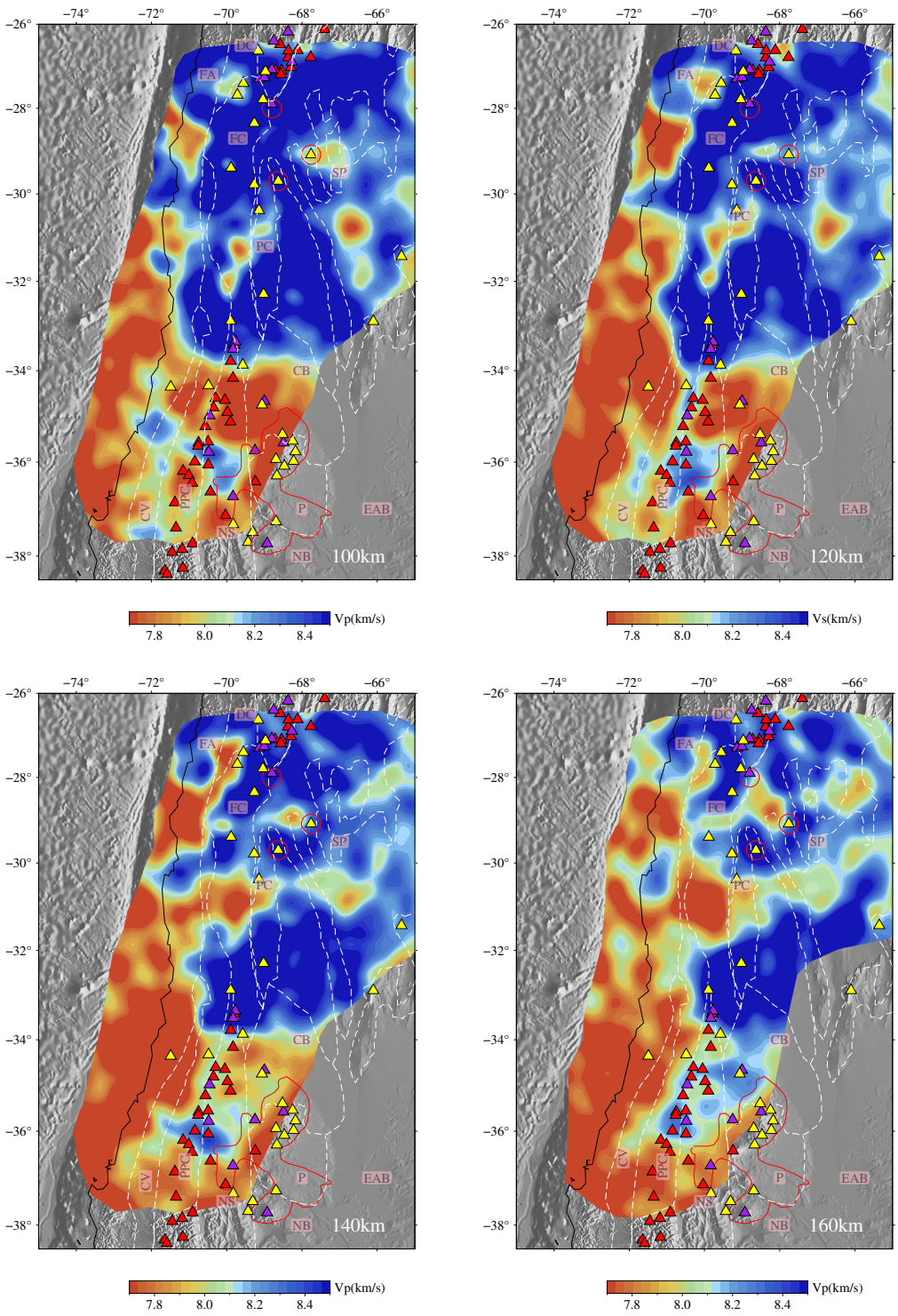

Figure S10. Horizontal slices for isotropic V_P model at 100 km, 120 km, 140 km and 160 km depth.

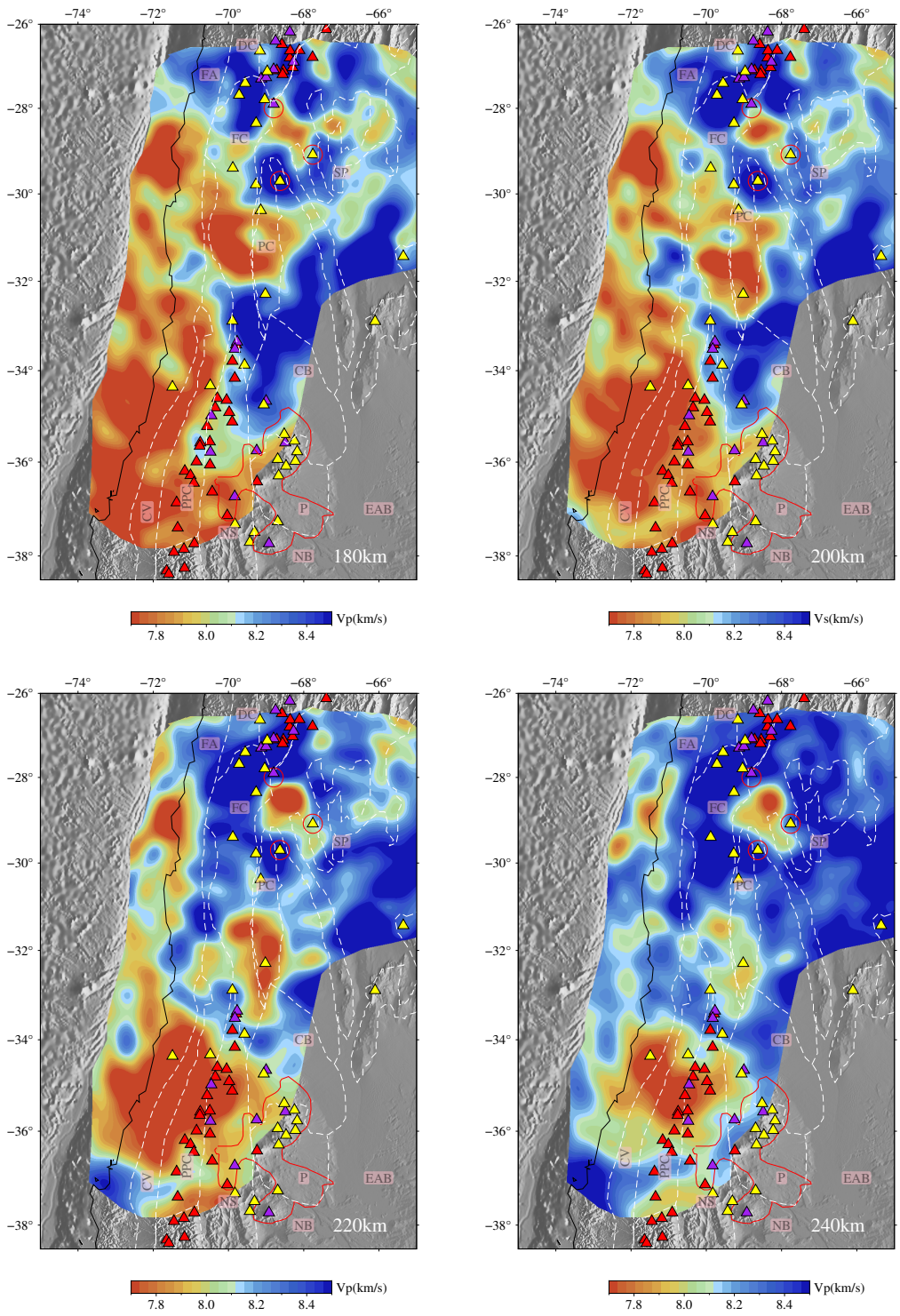

Figure S11. Horizontal slices for isotropic V_P model at 180 km, 200 km, 220 km and 240 km depth.

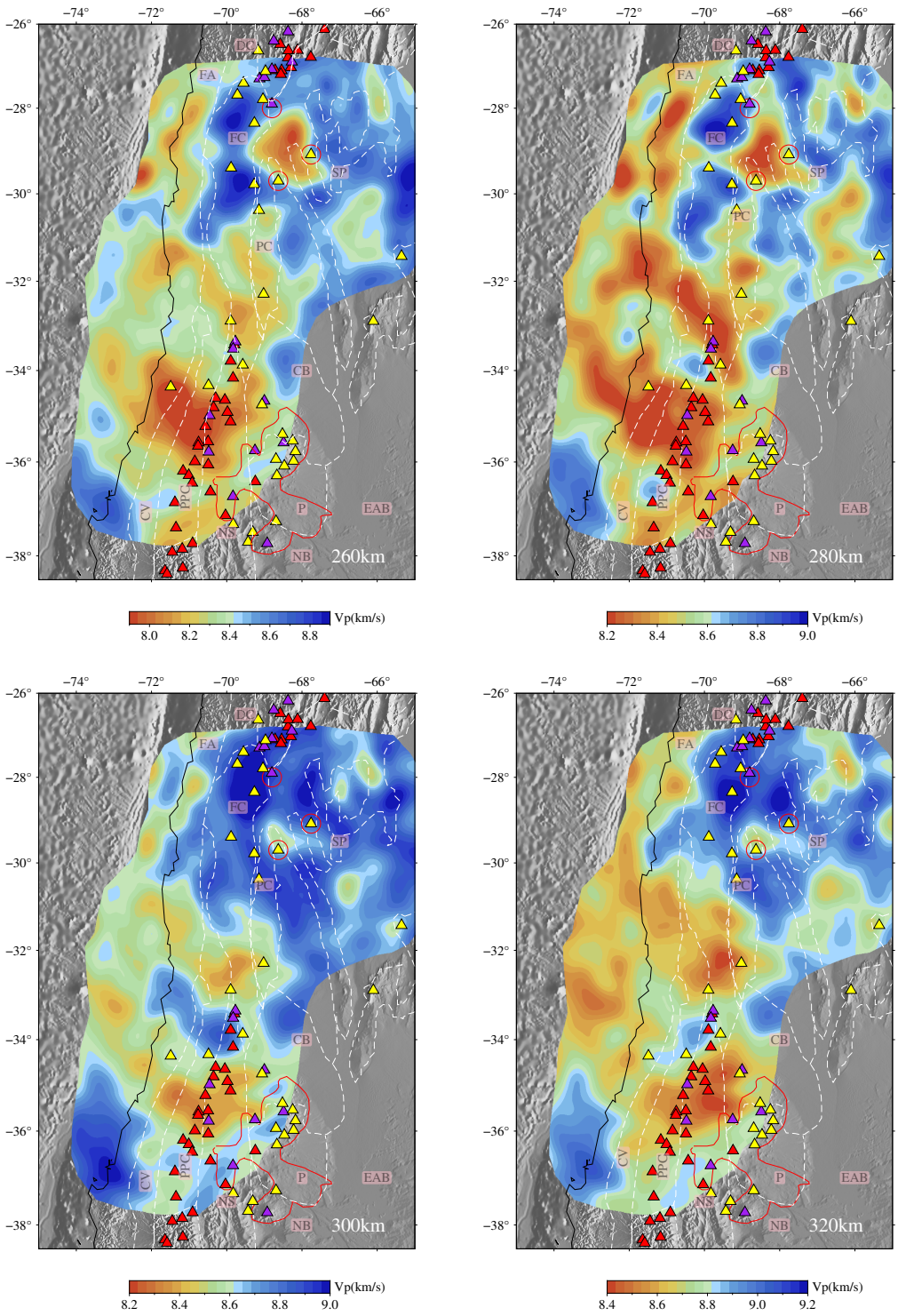

Figure S12. Horizontal slices for isotropic V_P model at 260 km, 280 km, 300 km and 320 km depth.

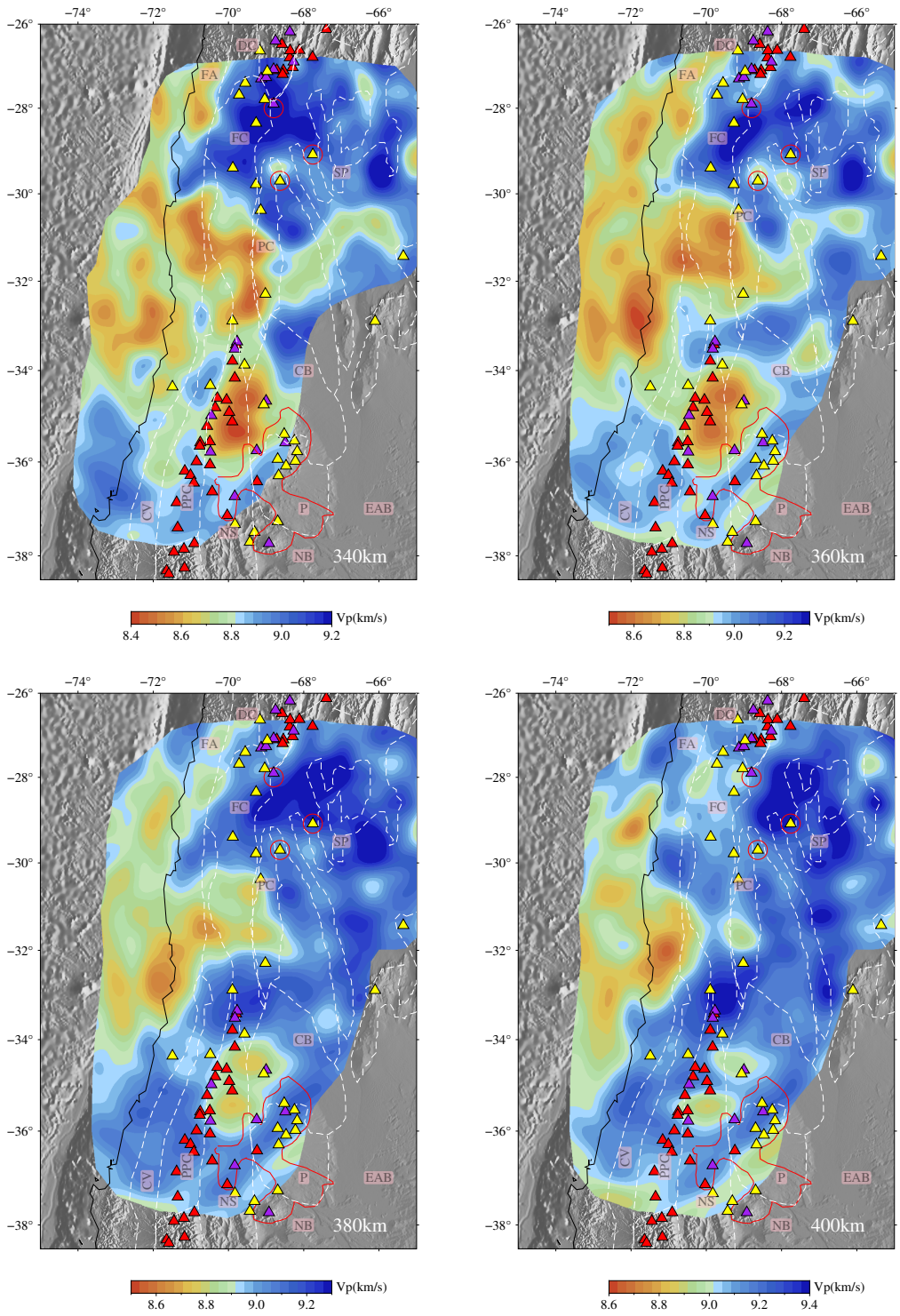

Figure S13. Horizontal slices for isotropic V_P model at 340 km, 360 km, 380 km and 400 km depth.

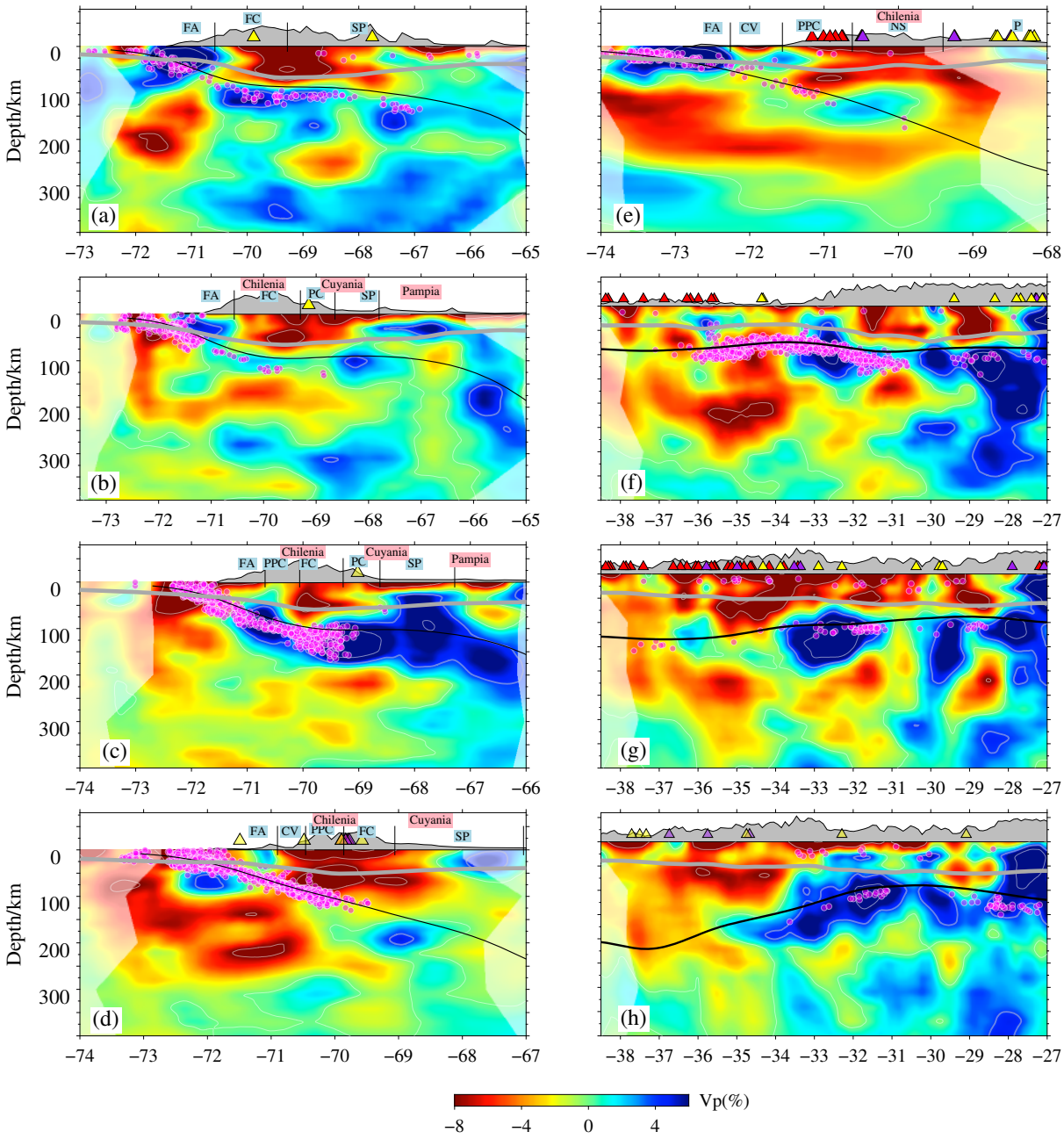

Figure S14. Cross-sections of isotropic V_p perturbations relative to the reference 1D V_p. The positions for the cross sections are defined in Figure 2(d) (see main text). Thick solid gray lines denote the continental Moho (Rivadeneyra-Vera et al., 2019) and thin solid black lines denote the slab contour from Slab 2.0 (Hayes et al., 2018). Magenta dots in b-d denote the seismicity relocated by Sippl et al. (2020) and in other profiles are retrieved from ISC-EHB catalog.

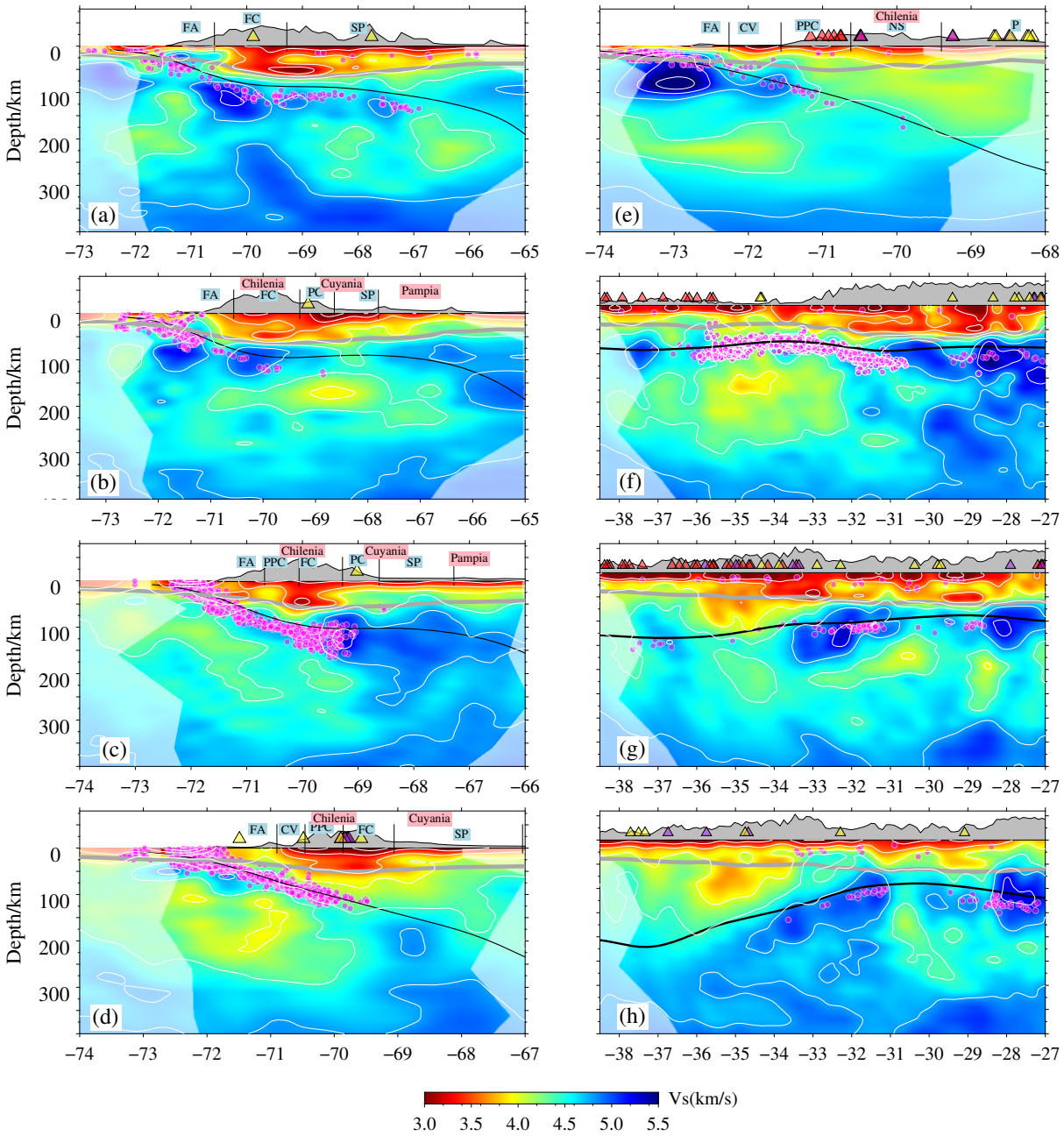

Figure S15. Isotropic absolute V_S cross-sections. For other figure elements see Fig. S14.

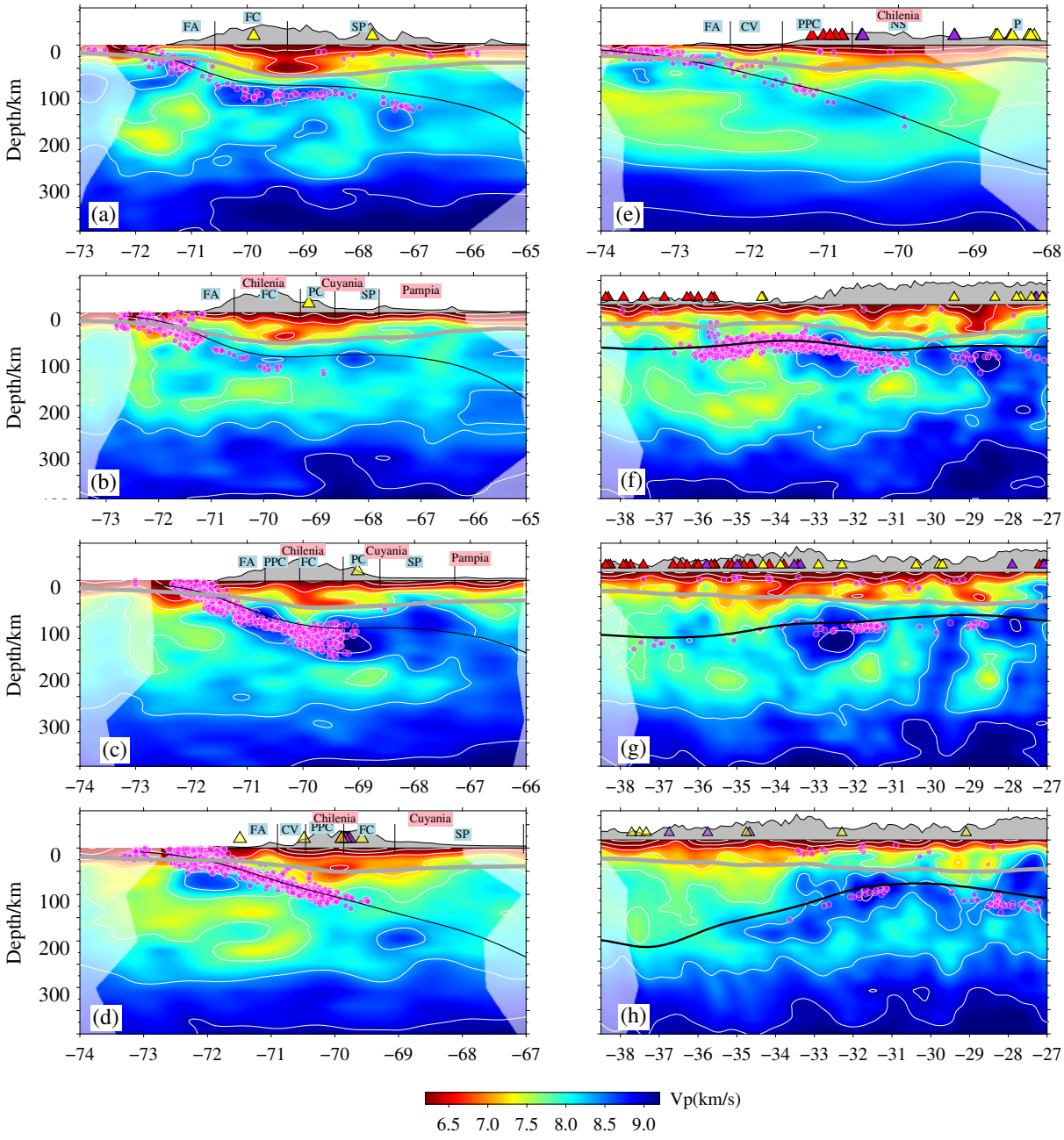

Figure S16. Isotropic absolute V_P cross-sections. For other figure elements see Fig. S14

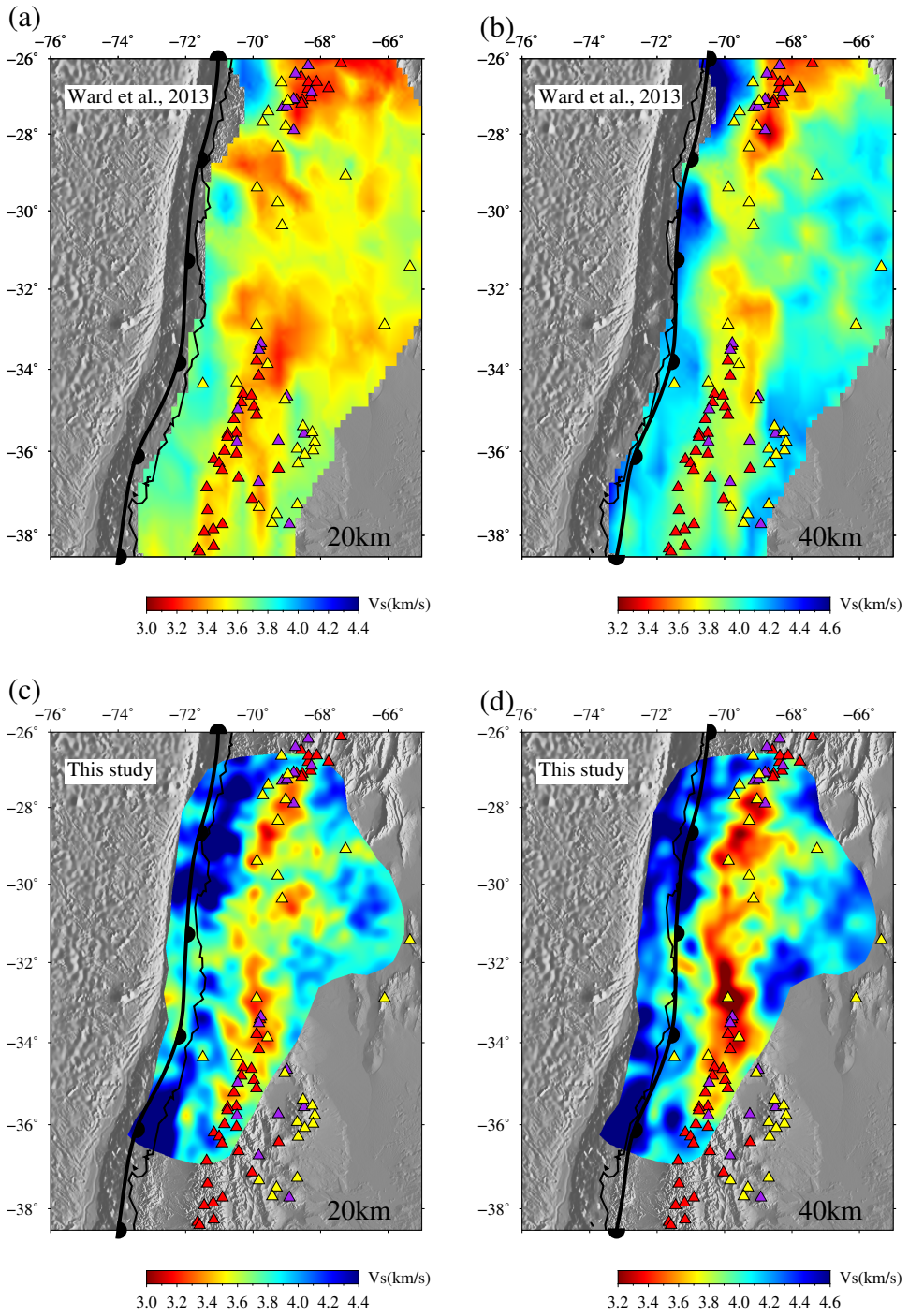

Figure S17. Comparison of the crustal structure inferred by the ambient noise tomography model of Ward et al. (2013) (top) with our model (bottom).

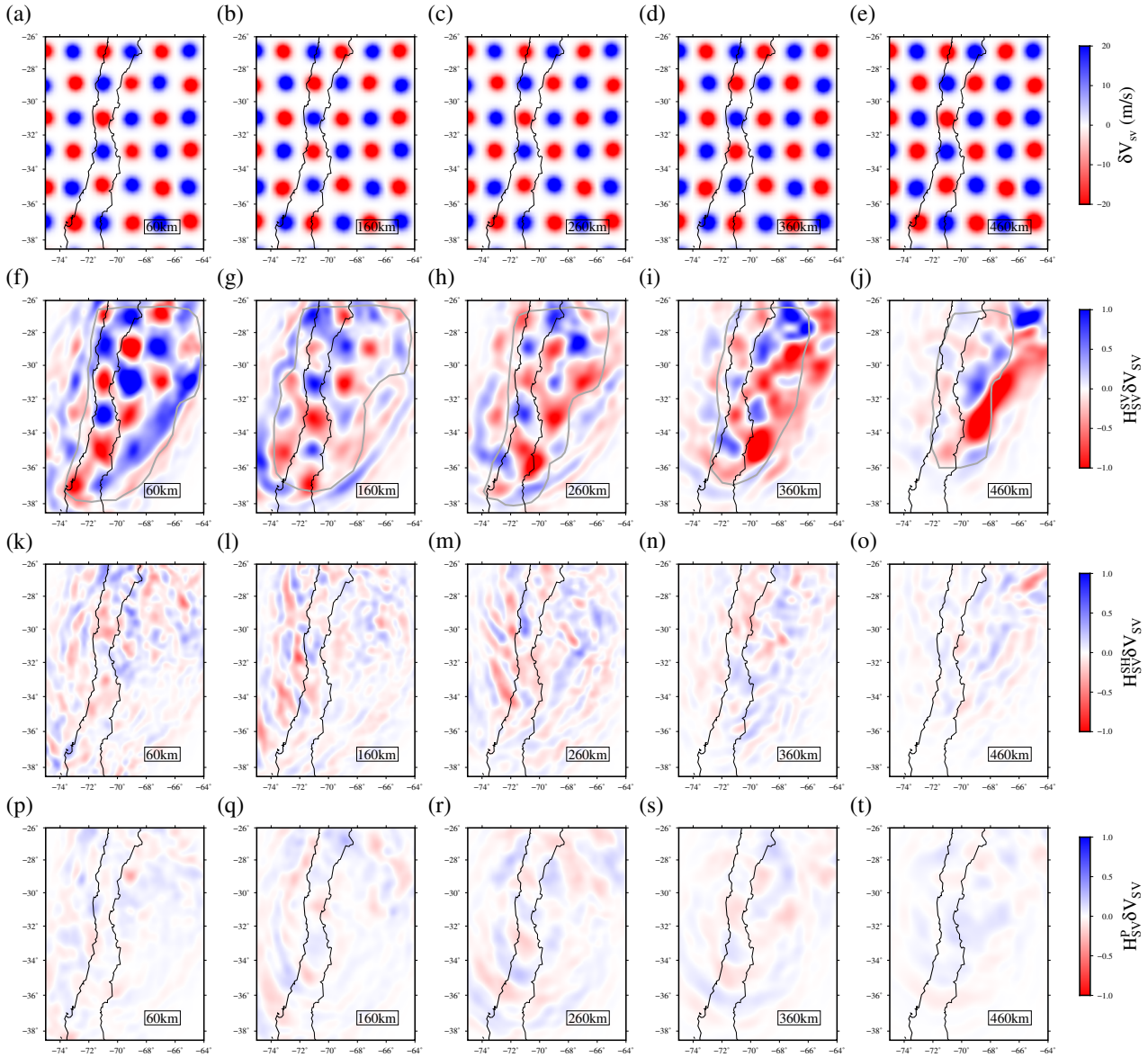

Figure S18. Point-spread function test with respect to $\mathbf{V}_{SV}$ perturbations ($\delta\mathbf{V}_{SV}$). (a-e): horizontal slices of input 1% Gaussian $\mathbf{V}_{SV}$ perturbations ($\delta\mathbf{V}_{SV}$) with σ=40 km at 60 km, 160 km, 260 km, 360 km and 460 km depth in the upper mantle; (f-j): point-spread functions $\mathbf{H}_{SV}^{SV}\delta\mathbf{V}_{SV}$ with respect to V_{SV} perturbations ($\delta\mathbf{V}_{SV}$) quantify the resolution for V_{SV}. (k-o): point-spread functions $\mathbf{H}_{SV}^{SH}\delta\mathbf{V}_{SV}$ quantify the cross-talk between V_{SV} and V_{SH}; (p-t) point-spread functions $\mathbf{H}_{SV}^{P}\delta\mathbf{V}_{SV}$ quantify the trade-off between V_{SV} and V_P. Gray thick lines in f-j denote the trust region for $\mathbf{V}_{SV}$ used for masking results plots.

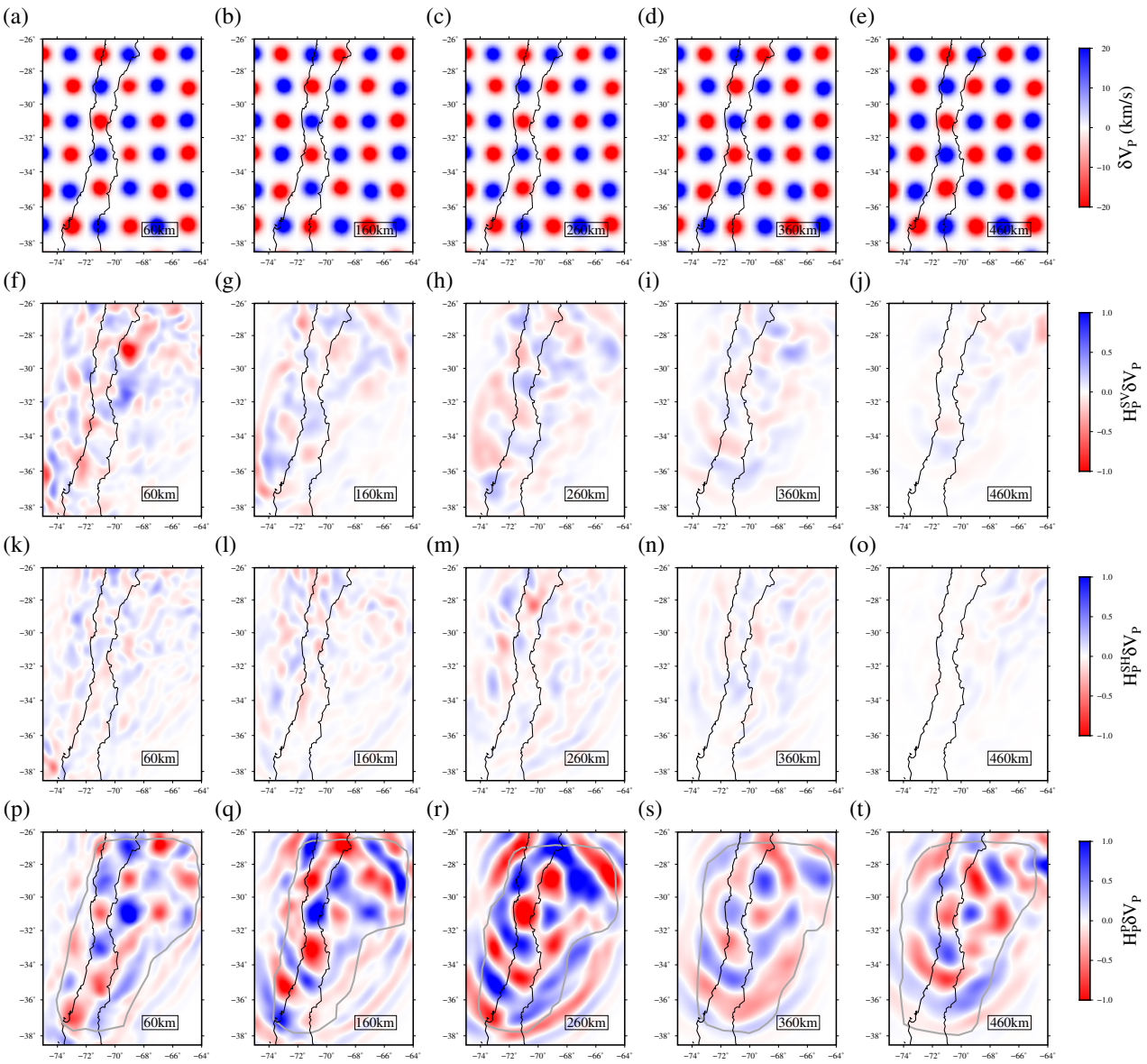

Figure S19. Point-spread function test with respect to isotropic $\mathbf{V}_P$ perturbations ($\delta\mathbf{V}_P$). (a-e): horizontal slices of input 1% Gaussian $\mathbf{V}_P$ perturbations ($\delta\mathbf{V}_P$) with σ=40 km at 60 km, 160 km, 260 km, 360 km and 460 km depth in the upper mantle; (f-j): point-spread functions $\mathbf{H}_P^{SV}\delta\mathbf{V}_P$ with respect to isotropic V_P perturbations ($\delta\mathbf{V}_P$); (k-o): point-spread functions $\mathbf{H}_P^{SH}\delta\mathbf{V}_P$; (p-t) point-spread functions $\mathbf{H}_P^{P}\delta\mathbf{V}_P$; Gray thick lines denote the trust region for $\mathbf{V}_P$.

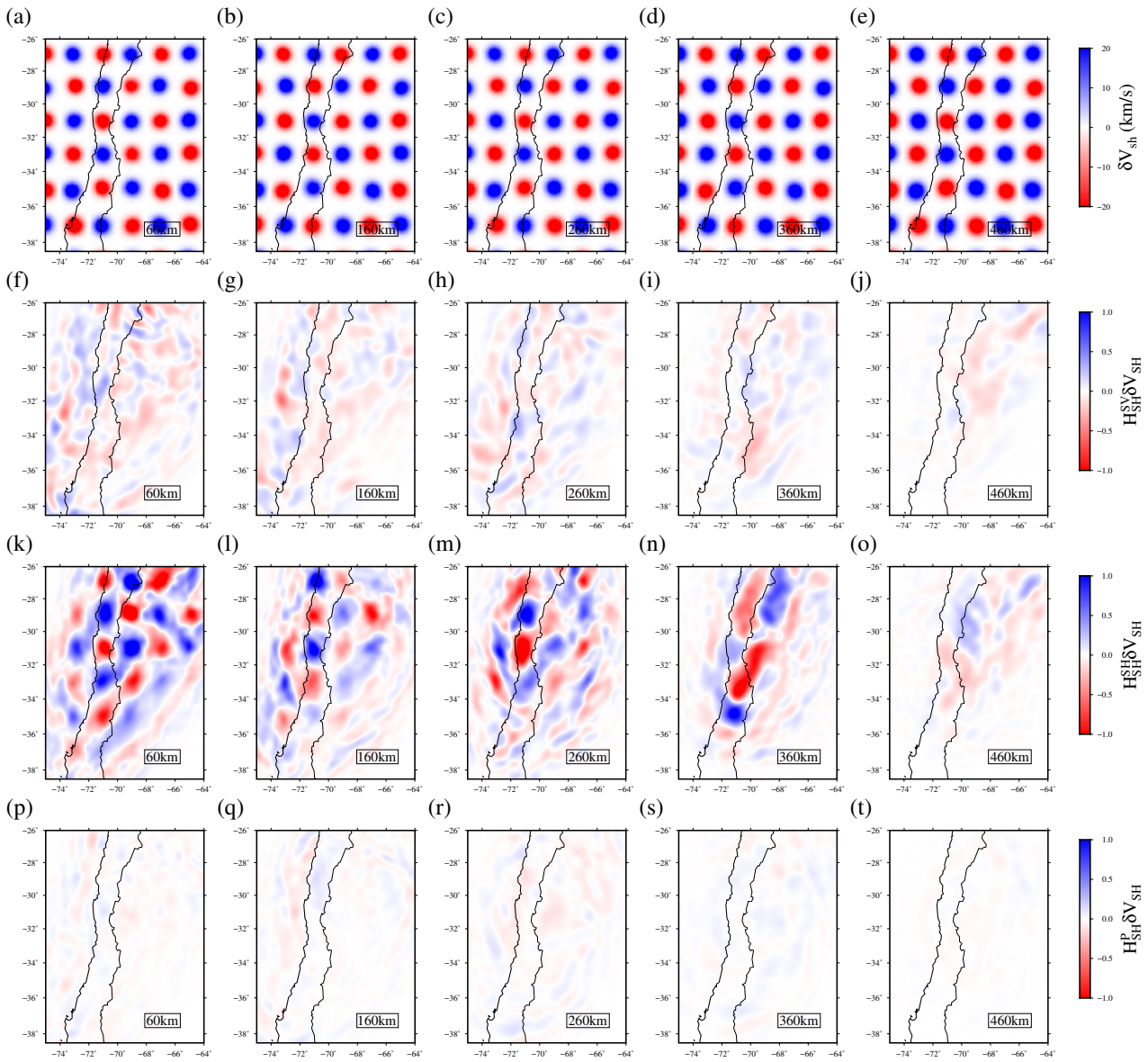

Figure S20. Point-spread function test with respect to $\mathbf{V}_{SH}$ perturbations ($\delta\mathbf{V}_{SH}$). (a-e): horizontal slices of input 1% Gaussian $\mathbf{V}_{SH}$ perturbations ($\delta\mathbf{V}_{SH}$) with σ=40 km at 60 km, 160 km, 260 km, 360 km and 460 km depth in the upper mantle; (f-j): point-spread functions $\mathbf{H}_{SH}^{SV}\delta\mathbf{V}_{SH}$ with respect to V_{SH} perturbations ($\delta\mathbf{V}_{SH}$); (k-o): point-spread functions $\mathbf{H}_{SH}^{SH}\delta\mathbf{V}_{SH}$; (p-t) point-spread functions $\mathbf{H}_{SH}^{P}\delta\mathbf{V}_{SH}$.

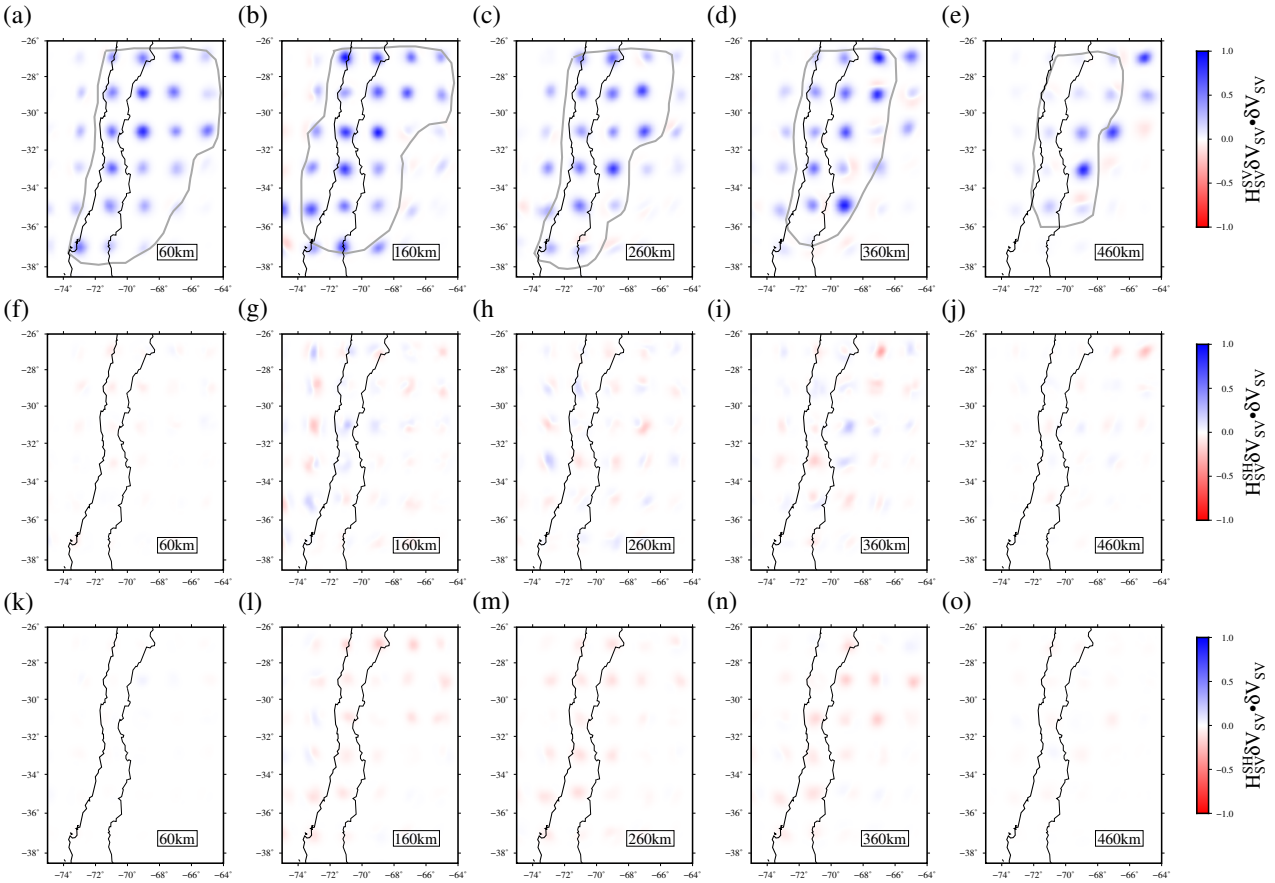

Figure S21. Normalised product between the $\delta\mathbf{V}_{SV}$ and point-spread functions $\mathbf{H}_{SV}^{SV}\delta\mathbf{V}_{SV}$ (a-e), $\mathbf{H}_{SV}^{P}\delta\mathbf{V}_{SV}$ (f-j) and $\mathbf{H}_{SV}^{SH}\delta\mathbf{V}_{SV}$ (k-o). All the results are normalised by the product of the maximum of $\delta\mathbf{V}_{SV}$ and the maximum of $\mathbf{H}_{SV}^{SV}\delta\mathbf{V}_{SV}$ for every depth level. The best resolution is indicated by blue dots of uniform amplitude for the same anomaly type (a-e); poor resolution by uneven recovery or red zones indicates failure to recover the basic anomalies. For perfect resolution the plots in f-o would be uniformly white; in fact minor cross-talk of parameters is observed. Note that this test focuses attention on recovery of correct anomaly polarities in the anomaly centres, giving a clearer picture in this regard than the raw checkerboard point spread recovery results, but that the importance of smearing effects is not visible. Both visualisations are therefore best considered together.

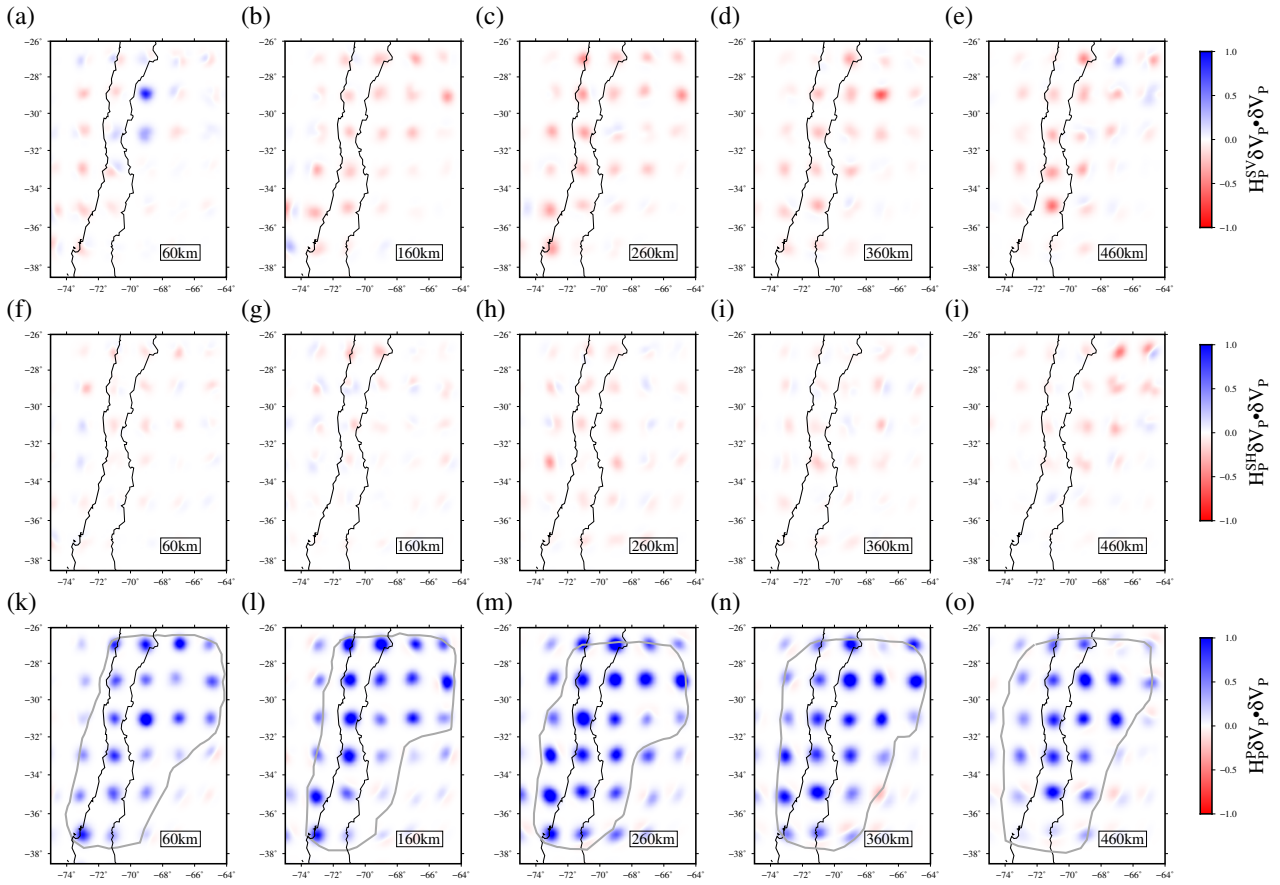

Figure S22. Normalised product between the $\delta \mathbf{V}_P$ and point-spread functions $\mathbf{H}_{SV}^{P}\delta \mathbf{V}_P$ (a-c), $\mathbf{H}_{P}^{SH}\delta \mathbf{V}_P$ (d-f) and $\mathbf{H}_{P}^{P}\delta \mathbf{V}_P$ (g-i). All the results are normalised by the product of the maximum of $\delta \mathbf{V}_P$ and the maximum of $\mathbf{H}_{P}^{P}\delta \mathbf{V}_P$ for every depth level.

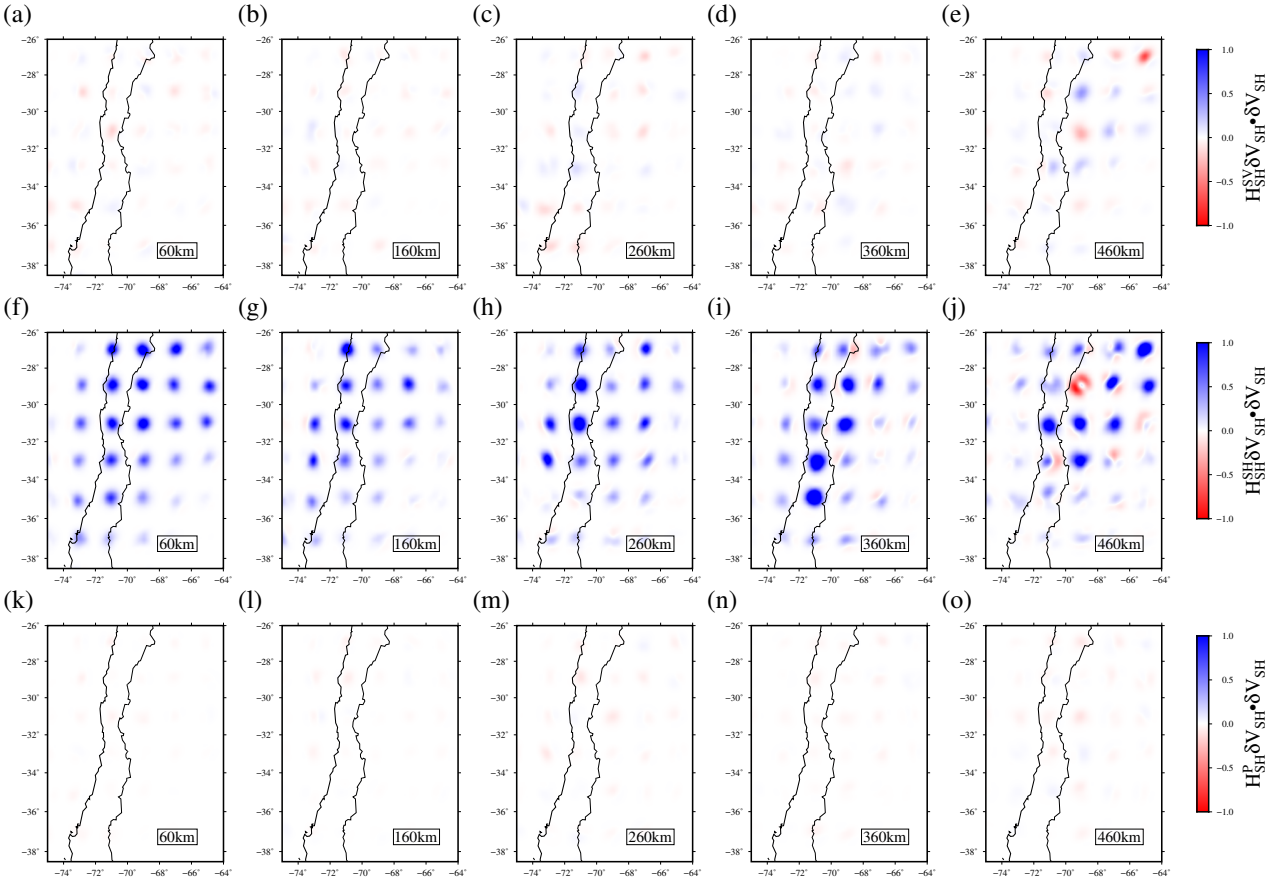

Figure S23. Normalised product between the $\delta \mathbf{V}_{SH}$ and point-spread functions $\mathbf{H}^{SH}_{SV}\delta \mathbf{V}_{SH}$ (a-c), $\mathbf{H}^{SH}_{SH}\delta \mathbf{V}_{SH}$ (d-f) and $\mathbf{H}^{SH}_{P}\delta \mathbf{V}_{SH}$ (g-i). All the results are normalised by the product of the maximum of $\delta \mathbf{V}_{SH}$ and the maximum of $\mathbf{H}^{SH}_{SH}\delta \mathbf{V}_{SH}$ for every depth level.

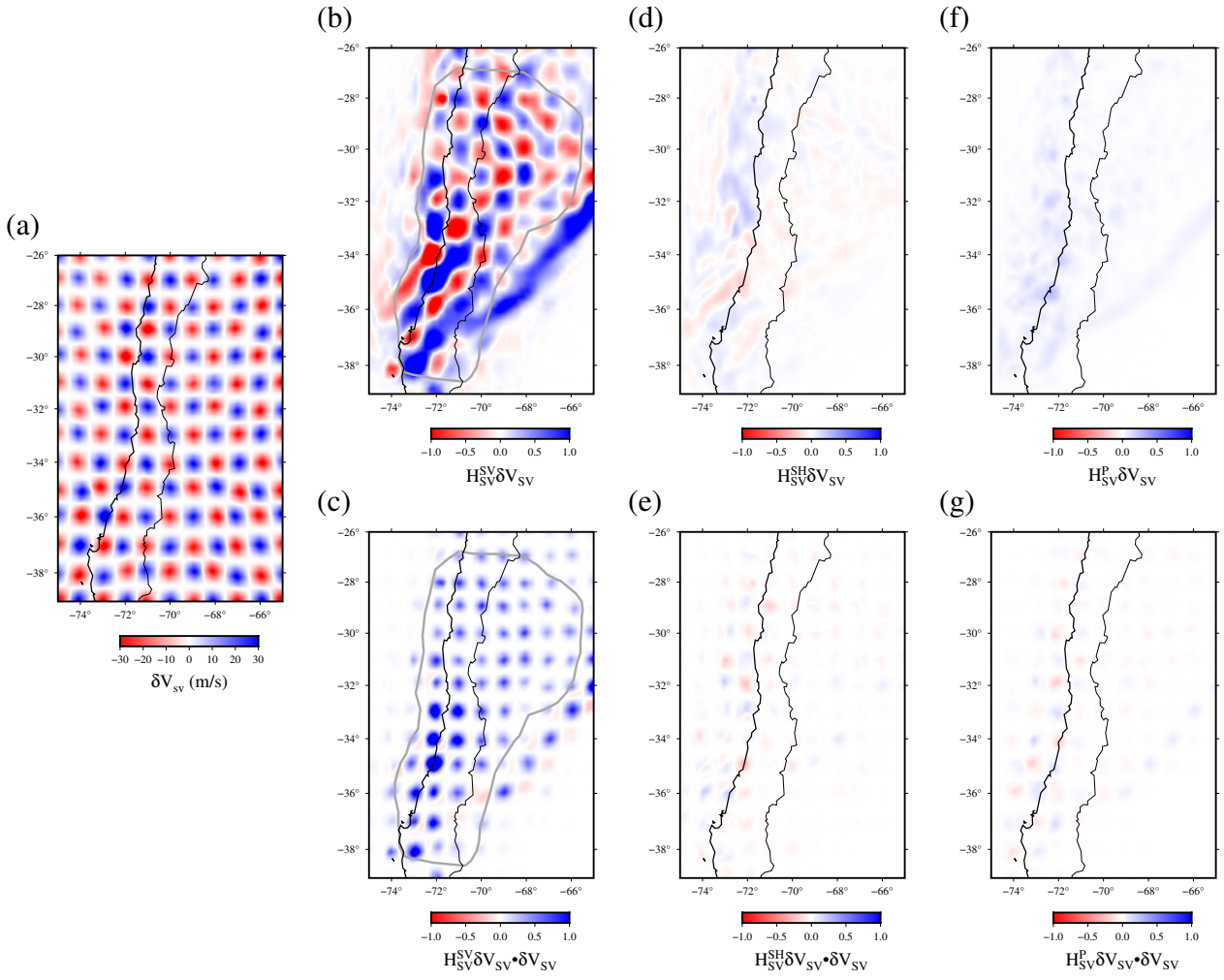

Figure S24. (a) Horizontal slice of input 1% Gaussian $\mathbf{V}_{SV}$ perturbations ($\delta\mathbf{V}_{SV}$) with σ=25 km at 20 km depth in the crust; (b), (d), (f) point-spread functions $\mathbf{H}^{SV}_{SV}\delta\mathbf{V}_{SV}$, $\mathbf{H}^{SH}_{SV}\delta\mathbf{V}_{SV}$, $\mathbf{H}^{P}_{SV}\delta\mathbf{V}_{SV}$ with respect to V_{SV} perturbations ($\delta\mathbf{V}_{SV}$), respectively. (c), (e), (g) Normalised product between the $\delta\mathbf{V}_{SV}$ and point-spread functions $\mathbf{H}^{SV}_{SV}\delta\mathbf{V}_{SV}$, $\mathbf{H}^{SH}_{SV}\delta\mathbf{V}_{SV}$, $\mathbf{H}^{P}_{SV}\delta\mathbf{V}_{SV}$, respectively. All the products are normalised by the product of the maximum of $\delta\mathbf{V}_{SV}$ and the maximum of $\mathbf{H}^{SV}_{SV}\delta\mathbf{V}_{SV}$

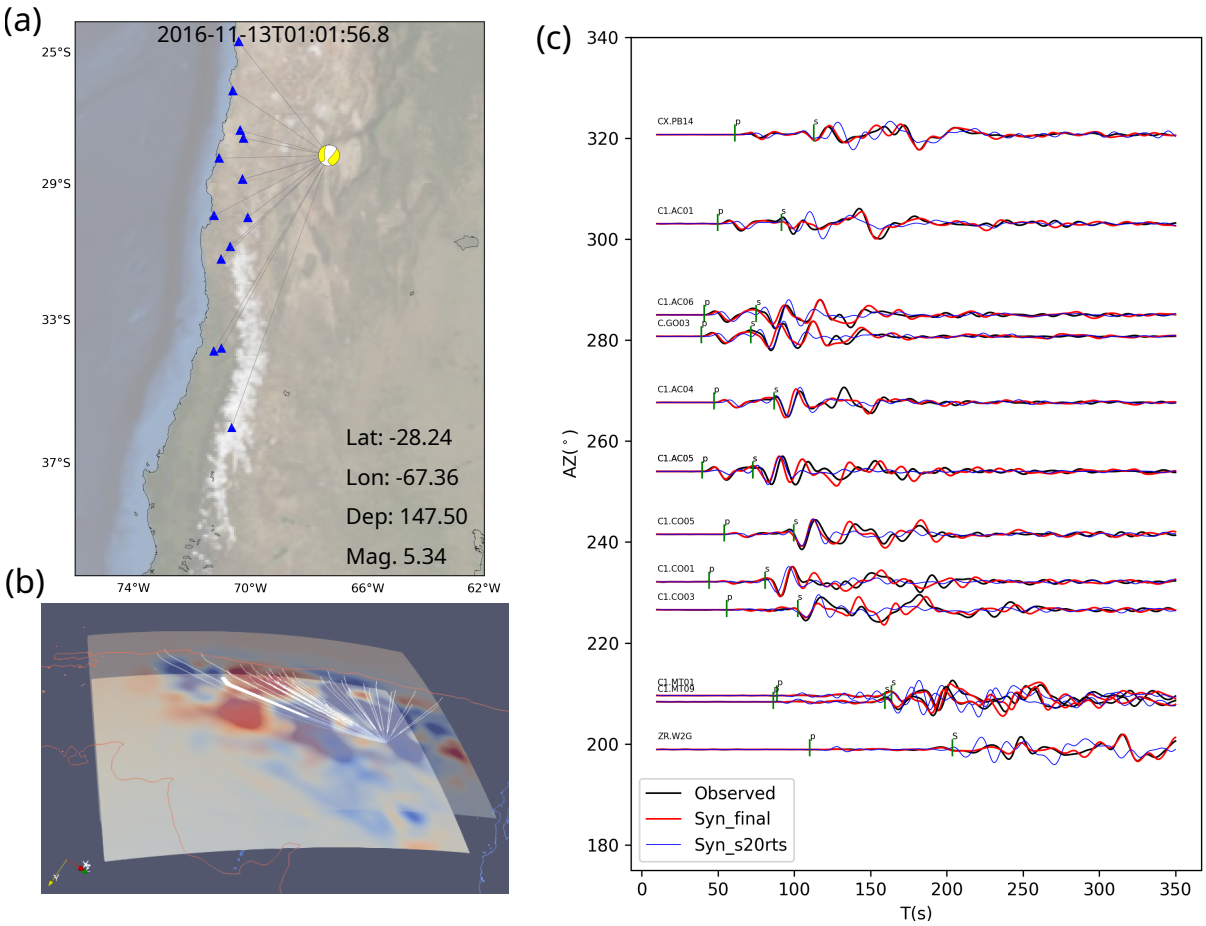

Figure S25. Waveform comparison between the initial and final model for Z component. (a) Map for example event (centroid depth 148 km) and stations. (b) 3D ray-path illustration. (c) Observed (black lines) and synthetic waveforms (blue: initial model - S20RTS; red: final model) for the indicated stations. Ray-path and arrival times are predicted for IASP91 using Taup toolkit in Obspy.

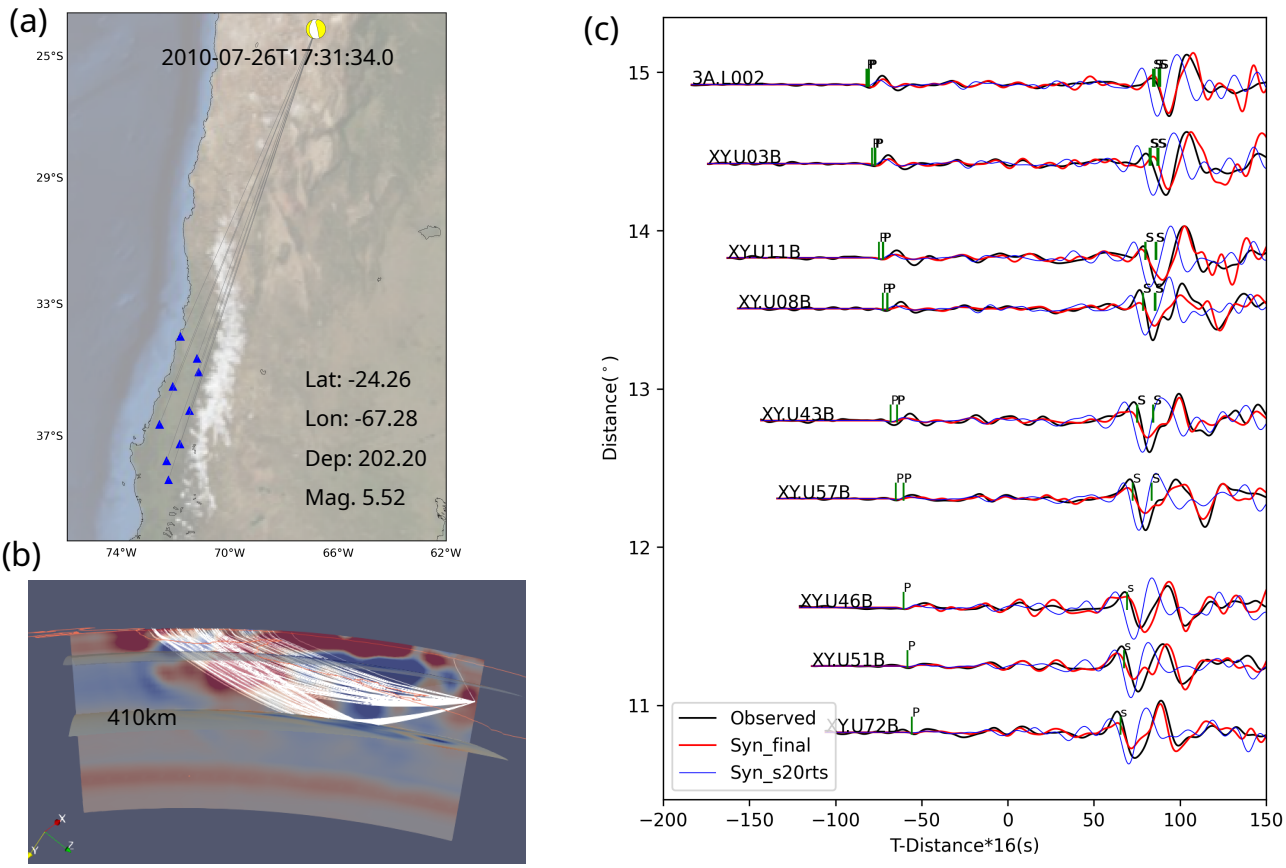

Figure S26. Waveform comparison for example event at centroid depth 202 km. For other figure elements see Fig. S25.

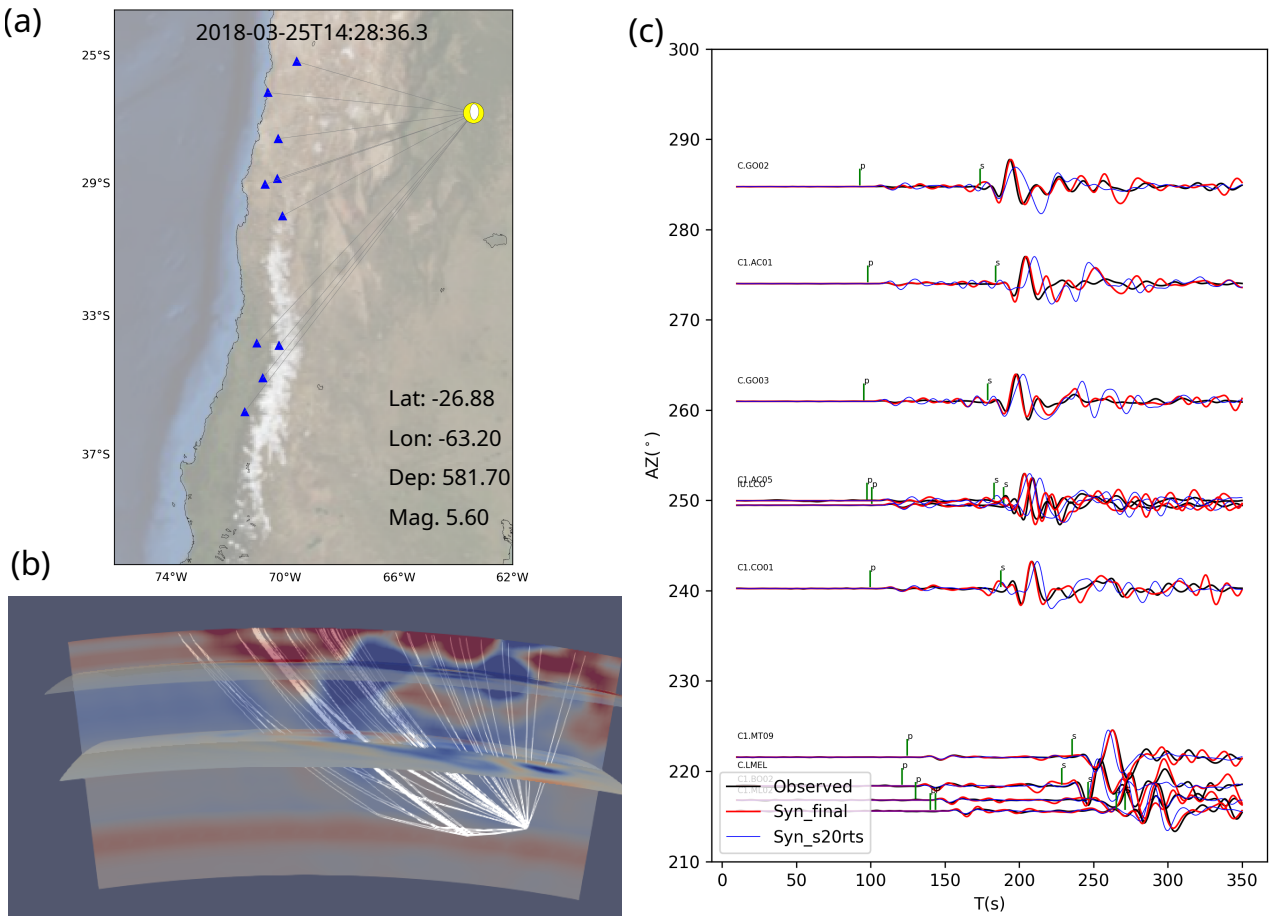

Figure S27. Waveform comparison for example event at centroid depth 582 km. For other figure elements see Fig. S25.

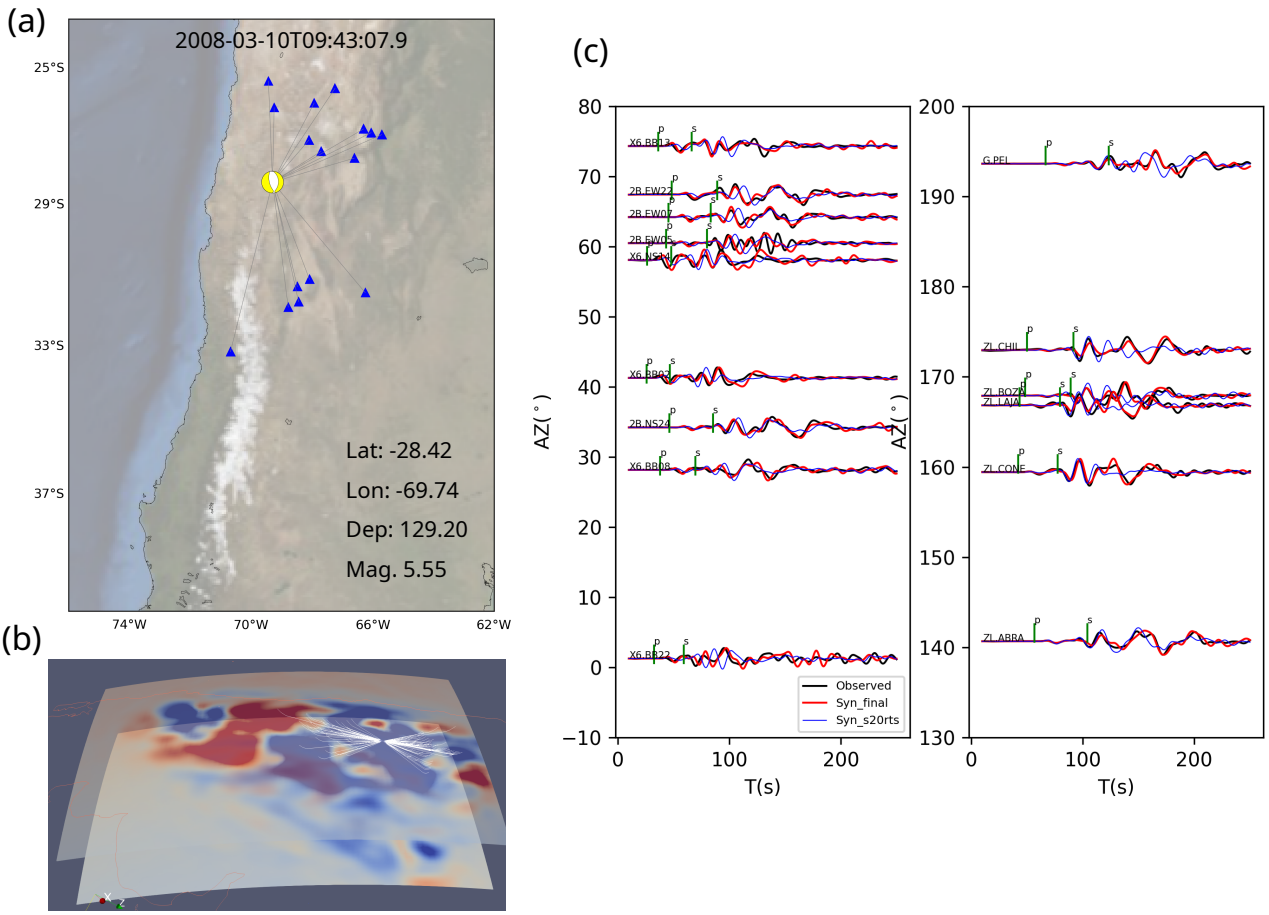

Figure S28. Waveform comparison for example event at centroid depth 129.20 km. For other figure elements see Fig. S25.